FLUID SUBSTITUTION AND AVAZ ANALYSIS OF FRACTURED DOMAINS: AN ULTRASONIC EXPERIMENTAL STUDY

A Thesis

Presented to

the Faculty of the Department of Earth and Atmospheric Sciences

University of Houston

In Partial Fulfillment

of the Requirements for the Degree

Master of Science

By

Long Huang

August, 2013

FLUID SUBSTITUTION AND AVAZ ANALYSIS OF FRACTURED DOMAINS: AN ULTRASONIC EXPERIMENTAL STUDY

Long Huang

APPROVED:

Dr. Robert Stewart, Committee Chair
Department of Earth and Atmospheric Sciences

Dr. Evgeny Chesnokov, Committee member
Department of Earth and Atmospheric Sciences

Dr. Samik Sil, Committee member
ConocoPhillips

Dean
College of Natural Sciences and Mathematics

Acknowledgements

First, I would like to express my sincere gratitude to my advisor Dr. Robert Stewart for his enthusiastic supervision, for his insightful suggestions on my research, and for his willingness to share his wisdom with me. And I believe that it will benefit me for life.

I would like to gratefully acknowledge the other committee members Dr. Evgeny Chesnokov, Dr. Samik Sil, and Dr. Leon Thomsen who was formerly my committee member for their invaluable assistance, guidance, and support. Without their great knowledge and expertise in different fields this thesis would not be possible.

Special thanks go to Dr. Nikolay Dyaur, who helped and kept teaching me during the ultrasonic measurements and experiments. Without his help, I would not have finished my thesis in time. I would like to thank Bode Ommoboya, Tao Jiang, and Anoop Williams for their assistance and discussions.

Also, I'm very grateful to SEG Foundation and Dr. Robert Sheriff who supported my first-year research with their generous fellowship. Thanks to Allied Geophysical Laboratories and ConocoPhillips for their expertise, enthusiasm, and financial support of this work.

Finally, I would like to thank my family for supporting me and believing in me as always.

FLUID SUBSTITUTION AND AVAZ ANALYSIS OF FRACTURED DOMAINS: AN ULTRASONIC EXPERIMENTAL STUDY

An Abstract of a Thesis

Presented to

the Faculty of the Department of Earth and Atmospheric Sciences

University of Houston

In Partial Fulfillment

of the Requirements for the Degree

Master of Science

By

Long Huang

August, 2013

Abstract

Many regions of subsurface interest are, or will be, fractured. Seismic characterization of these zones is a complicated, but essential, task for resource development. Physical modeling, using ultrasonic sources and receivers over scaled exploration targets, can play a useful role as an analogue for reservoir characterization. The goal of this thesis is to understand and characterize fractured regions using physical models. Two physical models, with domains of aligned vertical fractures (HTI symmetry), are studied here. Through ultrasonic measurements, their elastic properties are measured and calculated. The first model is a glass block with an internal laser-etched fracture zone. Azimuthal CMP gathers are surveyed over the fracture zone with star-shooting pattern and multicomponent data are recorded with ultrasonic transducers. Using low frequency transducers, and small crack spacing relative to source frequency, target fracture zones behaves as an effective medium. Reflections from the fracture zone interfaces are carefully processed so that the true amplitudes of reflected signals are recovered. By AVO and AVAZ analysis, fracture orientation is estimated. The second model studied in this thesis is a 3D-printed model. Since the model material is porous, and we are interested in fluid effects, we saturate it with water. Significant changes after saturation are observed as P-wave velocity increase by 4.6% and S-wave velocity decrease by 1.6%. Thomsens parameters $\boldsymbol{\epsilon^V}$ and $\boldsymbol{\delta^V}$ decrease 40% in magnitude while $\boldsymbol{\gamma^V}$ increase over 8%. To explain these changes, a new set of equations based on linear slip theory and Gassmann's equations are derived and tested with both synthetic and experimental data.The predictions of these new equations match observations closely.

Contents

List of Figures

List of Tables

Chapter 1

Introduction

"Many regions of subsurface interest are, or will be, fractured" (Stewart et al., 2013). To seismically characterize these zones is a complicated, but essential, task for resource development. Physical modeling, using ultrasonic sources and receivers over scaled exploration targets, can play a useful role as a simulation for reservoir characterization. The goal of this thesis study is to characterize fractured regions by using physical models.

In physical modeling, Ebrom et al. (1990) and Tatham et al. (1992) employed stacked Plexiglas plates and ultrasonic measurements to simulate an effective anisotropic fractured medium. Cheadle et al. (1991) used industrial phenolic laminates to incorporate anisotropy into their observations. Rathore et al. (1995) prepared and surveyed an anisotropic synthetic sandstone with known crack geometry and dimension. These studies use largely homogeneous anisotropic materials. A recent physical modeling study (Stewart et al., 2013) introduced a novel laser-etching

technique to create fractured regions in a isotropic homogeneous glass block. Inspired from this laser-etching glass model, which is designed to investigate scattering imaging, a similar glass model is made which has smaller fracture spacing so that the fractured region is acting as an effective medium. Different kinds of seismic surveys are designed to try to characterize the fractures from seismic.

Another exciting new technology that attracts our eyes is the 3D printing (or additive manufacturing). This new technology allows us to print almost any physical models we can imagine. Segerman (2012) used 3D printing to visualise complex mathematical models. Calì et al. (2012) showed a number of articulated models with 3D printing. Lemu and Kurtovic (2012) studied the in-built potentials and limitations of 3D printing technology when used for rapid manufacturing purposes. They point out that a major weakness of 3D printing is the porosity introduced by the printing mechanism. However, this "problem" seems rather as an advantage to us as it creates porosity which is seen in most rocks. In this case, we believe we can manufacture artificial rocks and build them close to theoretical rock physics models. This idea is most useful in testing theoretical models such as Hudson's penny-shaped models (Hudson, 1981), Kuster-Toksz's model (Kuster and Toksz, 1974), and linear slip models (Schoenberger and Sayers, 1995). In this thesis, a linear slip 3D printed model is manufactured and tested with experiments.

1.1 Motivation

Physical modeling is a very useful tool for research in wave propagation and verification of theories. The reason for using physical modeling instead of numerical modeling or real field surveys is based on the following factors:

1. Cost. Physical modeling costs little compared to real field surveys and numerical modeling. The cost for numerical modeling depends on the algorism complexity, data size, and computer processing speed. Simple modeling is easy and really cheap; however, most numerical modeling is not cheap because the calculation takes a huge amount of time and you need better computers to run the calculation. Physical modeling requires less time and money. It usually takes about one or two days to prepare and run the surveys and the cost is just the models; typically the cost for these models vary from several hundred to maybe a few thousand dollars. Field surveys take months to prepare and millions of dollars for running; numerical modeling costs months for coding and days for the computers to run the calculation. In this way, physical modeling costs much less time and money which is really great for research.

2. Repeatability. Physical modeling is highly repeatable and we can easily run the survey again and again and the conditions remain almost the same. This is also a significant advantage for numerical modeling which gives results based on algorithms and its definitely constant as long as the algorithms and conditions are the same. Field surveys, however, may not be so repeatable, since the field is changing from time to time. The temperature is always different, the

pressure is fairly constant, and the wind speed and direction are changing, not to mention the cost for repeat the survey; all these factors make field surveys not so repeatable in practice.

3. Redesign. Usually we design our surveys based on our purpose and the data from a specific survey fit maybe one or two research purposes. For different research, we need different data and its not realistic to redesign the surveys in field. However, for physical modeling and numerical modeling, redesign is easy and in this case, we can record multiple dataset for different research purposes which is really important and useful for research.

4. Real materials and real waves. The reason for modeling is to simulate the real earth and get data from the simulation. We are trying to model the earth as much as we can, so it is very important if we can have real waves traveling through the real material. Physical modeling is definitely winning over numerical modeling for this part. Numerical modeling uses wave equations to simulate wave propagation and currently the wave equations we have are not perfect. In this case, we are not simulating the real earth, which instead puts a question mark to the results from numerical modeling.

5. Seismic band. Physical modeling is a scaled model for the real earth and in this case, most things are scaled and we have to be careful. Unlike geological physical modeling, seismic physical modeling is trickier. We need to take care of the scaling factor for both special and temporal factors. The transducer central frequency varies from 100 kHz to 5MHz and the scaling factor we use

in lab is 1:10000. The seismic band in field is from 10 Hz to 100 Hz, and its not even a problem for numerical modeling. Physical modeling, however, the central frequency band after scaling is from 10 Hz to 500 Hz, which is not a good simulation for real seismic. So in order to simulate real seismic better, we need to select the transducer, carefully.

In summary, physical modeling is cheap and less time consuming, highly repeatable, and easy to redesign. It simulates the real earth with real material and waves and the frequency band can fit as long as we select the right transducer.

1.2 Thesis outline

First, we study the laser-etched glass model using surface seismic to try to get the fracture orientation in Chapter 2. We use all kinds of different components for source and receiver and acquire 7-component data. Then, according to the data quality, we process some of the data and look close at the AVO response from different azimuth. Through AVO/AVAZ analysis, we are able to estimate the fracture orientation. Then, in Chapter 3, we study the 3D printed models as synthetic rocks. Fluid substitution experiments are performed on these models and new equations are derived to predict and explain the fluid effects on rock properties. Finally in Chapter 4, we discuss the two projects and conclude.

Chapter 2

Laser-etched glass model

In this chapter, the laser-etched glass model is studied with ultrasonic experiments. Its elastic properties are calculated and stiffness matrix is inverted. From the stiffness matrix, the symmetry is estimated to be an HTI medium. These measurements can be regarded as rock physics study which could help in reservoir characterization from seismic. We make multi-component surveys and process the data to get more information about the fracture zone. From AVO/AVAZ analysis, we are able to extract the fracture orientation from seismic.

2.1 Model description and measurement

2.1.1 Laser-etched glass models

The idea for laser-etched fractures within glass was fist given by Stewart et al. (2013). The glass model we start with is an isotropic homogenous glass block. Then we use the novel laser-etching technique to create domains of fractures inside the glass. This laser-etching technique allows us to place the fractures very precisely. Actually the "fractures" we talk about here are many small dots or crack bursts in the glass and they each become fault planes. Figure 2.1 shows the dimension of the glass model we use; we name this model as C11 (Figure 2.2). The model is a 400×220×120 mm glass block with a fractured zone 140×140×36 mm centered from top view. For the model we use in our study, we have 281 vertical fracture planes with 0.5 mm spacing (Figure 2.3). These vertical fracture planes create an HTI symmetry to the glass. The wavelength is estimated about 5.8 mm. So wavelength to fracture spacing ratio is about 12, which means we are working under effective medium domain rather than scattering.

2.1.2 Ultrasonic measurement

Our first measurements use direct transmission of energy across various faces of the glass blocks using 1 MHz transducers. The velocity for the blank (or unfractured) glass zones with path directions x, y, z had average values of $\boldsymbol{V_P}$= 5814 ms and $\boldsymbol{V_S}$= 3464 ms. From time picking and length measurement error, we estimate that

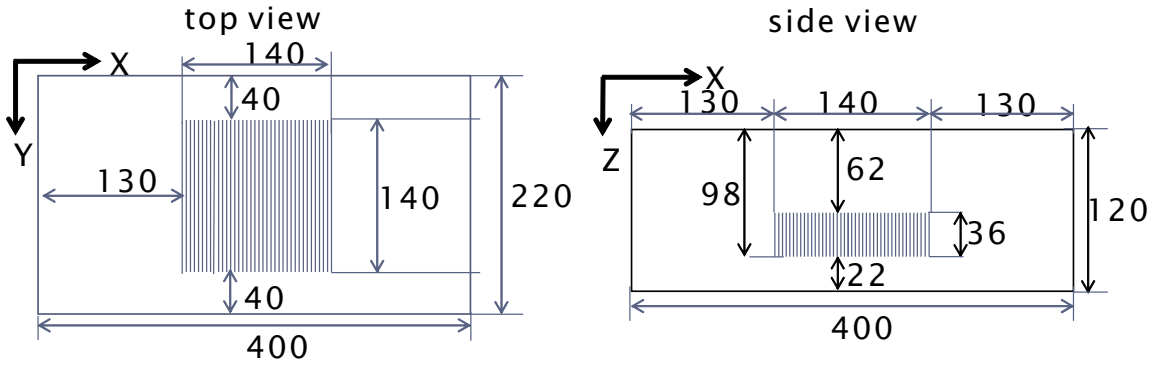

Figure 2.1: Schematic of the laser-etched glass model with dimensions.

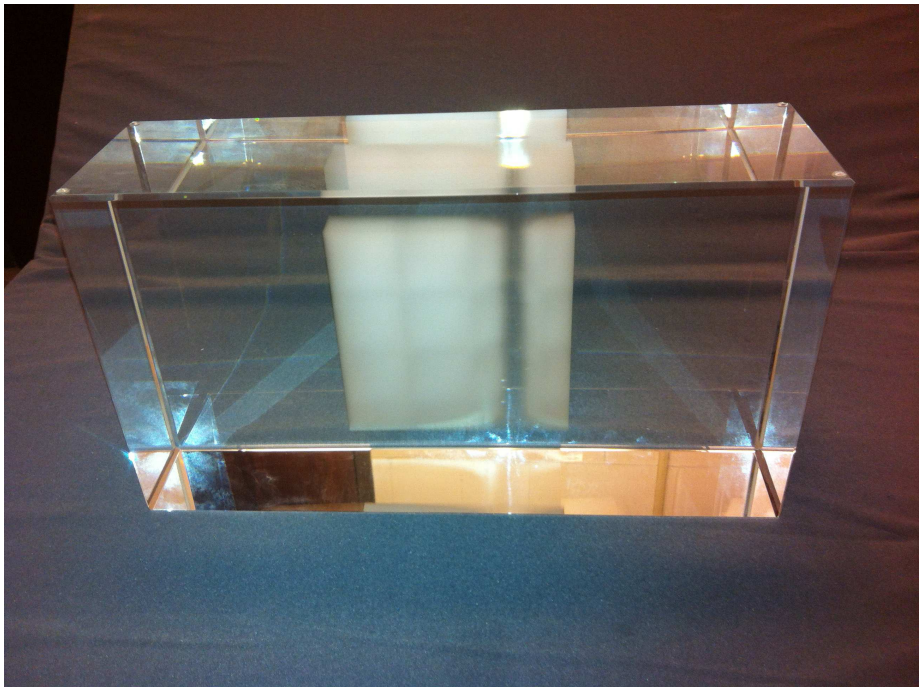

Figure 2.2: Glass model C11. The cloud inside the glass is the laser-etched fracture zone with 281 vertical fracture planes.

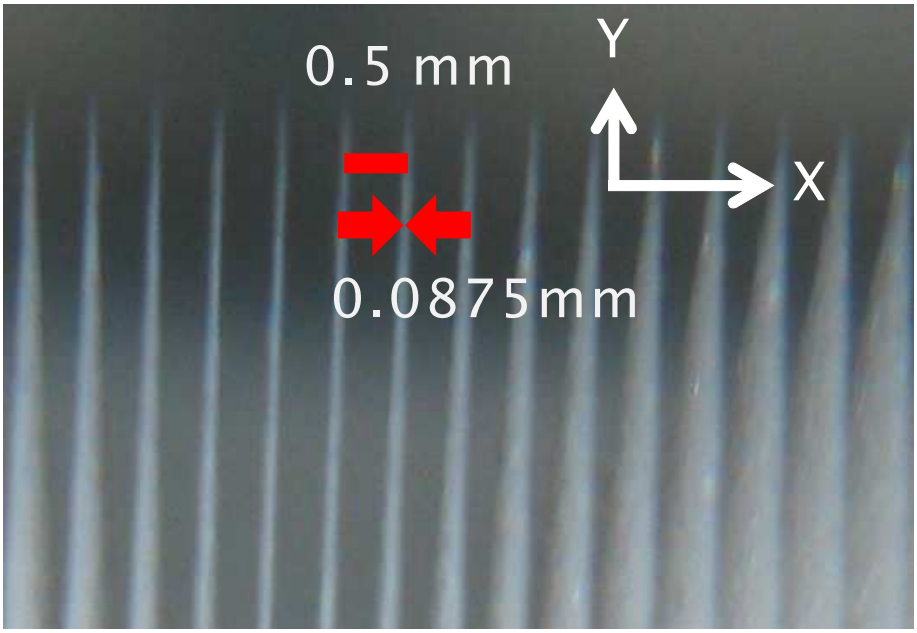

Figure 2.3: Laser-etched fracture planes. The fracture plane spacing is measured as 0.5 mm and the fracture layer thickness is about 0.09 mm.

the error in the calculated velocities ($\boldsymbol{V_P}$ and $\boldsymbol{V_S}$) was less than 0.03%. The average $\boldsymbol{V_P/V_S}$ value is 1.68. Table 2.1 shows velocities in different directions and for the fractured zone, we see velocity decrease in all directions. The horizontal P-wave velocity which travels normal to the fracture planes is 5702 m/s and the vertical P-wave velocity is about 5894 m/s; for the fast and slow velocity, the average fast shear wave velocity is $\boldsymbol{V_{S1}}$= 3458 m/s and the slow being $\boldsymbol{V_{S2}}$= 3418 m/s. The P-wave velocity for 45° is measured as $\boldsymbol{V_{P45}}$= 5745 m/s. The density of the glass model is 2.546 g/cc.

We know that the stiffness tensor (C) equals density ($\boldsymbol{\rho}$) times velocity square (Equation 2.1).

$$\boldsymbol{C = \rho V^2} \tag{2.1}$$

Direction	Vp (km/s)	Vs1 (km/s)	Vs2 (km/s)
X	5.814	3.463	
X-f	5.702	3.422	3.418
Y	5.813	3.465	
Y-f	5.766	3.456	3.417
Z	5.815	3.465	
Z-f	5.794	3.460	3.413

Table 2.1: Velocity for different directions. "-f" denotes in fractured zone.

For an HTI symmetry, we can represent the elastic stiffness as symmetric 6×6 matrix $\boldsymbol{C_{HTI}}$ (Rüger, 2001) as in Equation 2.2.

$$\boldsymbol{C_{HTI}} = \begin{pmatrix} \boldsymbol{C_{11}} & \boldsymbol{C_{13}} & \boldsymbol{C_{13}} & \boldsymbol{0} & \boldsymbol{0} & \boldsymbol{0} \\ \boldsymbol{C_{13}} & \boldsymbol{C_{33}} & \boldsymbol{(C_{33} - 2C_{44})} & \boldsymbol{0} & \boldsymbol{0} & \boldsymbol{0} \\ \boldsymbol{C_{13}} & \boldsymbol{(C_{33} - 2C_{44})} & \boldsymbol{C_{33}} & \boldsymbol{0} & \boldsymbol{0} & \boldsymbol{0} \\ \boldsymbol{0} & \boldsymbol{0} & \boldsymbol{0} & \boldsymbol{C_{44}} & \boldsymbol{0} & \boldsymbol{0} \\ \boldsymbol{0} & \boldsymbol{0} & \boldsymbol{0} & \boldsymbol{0} & \boldsymbol{C_{55}} & \boldsymbol{0} \\ \boldsymbol{0} & \boldsymbol{0} & \boldsymbol{0} & \boldsymbol{0} & \boldsymbol{0} & \boldsymbol{C_{55}} \end{pmatrix} \tag{2.2}$$

From the measured velocities and density, we calculate the stiffness matrix of the fractured zone (Equation 2.3).

$$\boldsymbol{C_{HTI}} = \begin{pmatrix} \boldsymbol{82.79} & \boldsymbol{84.03} & \boldsymbol{84.03} & \boldsymbol{0} & \boldsymbol{0} & \boldsymbol{0} \\ \boldsymbol{84.03} & \boldsymbol{85.48} & \boldsymbol{24.59} & \boldsymbol{0} & \boldsymbol{0} & \boldsymbol{0} \\ \boldsymbol{84.03} & \boldsymbol{24.59} & \boldsymbol{85.48} & \boldsymbol{0} & \boldsymbol{0} & \boldsymbol{0} \\ \boldsymbol{0} & \boldsymbol{0} & \boldsymbol{0} & \boldsymbol{30.44} & \boldsymbol{0} & \boldsymbol{0} \\ \boldsymbol{0} & \boldsymbol{0} & \boldsymbol{0} & \boldsymbol{0} & \boldsymbol{29.74} & \boldsymbol{0} \\ \boldsymbol{0} & \boldsymbol{0} & \boldsymbol{0} & \boldsymbol{0} & \boldsymbol{0} & \boldsymbol{29.74} \end{pmatrix} \boldsymbol{GPa} \tag{2.3}$$

We also calculate the Thomsen's parameters (Thomsen, 1986) for the HTI symmetry using the notation system defined by Rüger (2001).

$$\epsilon^V = \frac{C_{11} - C_{33}}{2C_{33}}, \tag{2.4}$$

$$\delta^V = \frac{(C_{13} + C_{55})^2 - (C_{33} - C_{55})^2}{2C_{33}(C_{33} - C_{55})}, \tag{2.5}$$

$$\gamma^V = \frac{C_{66} - C_{44}}{2C_{44}}, \tag{2.6}$$

We get ϵ^V= -0.031, δ^V= -0.034, γ^V= -0.012. Since $\epsilon^V \approx \delta^V$, the fractured zone can be characterized as elliptically anisotropic medium (Thomsen, 1986).

2.2 Ultrasonic survey experiments

The glass model simulates a three-layer earth model and we use ultrasonic transducer and land system to simulate seismic acquisition. The idea of the experiment is to try to identify fractured zones from seismic measurements. We start with two simple 2D lines one of which goes along the direction of the symmetry axis over fracture zone and the other over the the blank glass. By comparing the two profiles, we try to identify the reflections from the fracture zone. Then we extend to different azimuth, multi-component surveys and use these azimuthal multi-component data to characterize the fracture zone.

2.2.1 2D lines

The experiment was set up in the land system in Allied Geophysical Laboratories (AGL). In this system, we can use different transducers to work as source and receiver simulating on-shore data acquisition. Source and receiver offset is precisely controlled by the system and the data is recorded and stored in the computer. A scaling factor of 1:10000 for time and space upscaling (or for frequency downscaling) is used to make ultrasonic measurements more accessible to standard seismic values. For example, an actual 1.0 s pulse time in the lab is replotted as a 10 ms traveltime; a model dimension of 50 mm becomes 500 m. In this paper, we quote the original millimeter-scale lab dimensions and microsecond time measurements with some conversion to the associated seismic field scale. The glass used here is basically a dry, zero-porosity sandstone-type matrix and thus its ultrasonic properties (e.g., velocities) might be directly comparable to seismic values. If we scale the dimensions of the glass blocks by the 10,000 factor (ultrasonic to seismic), then the model area is about 4×2.2 km with a depth of 1.2 km.

We use one transducer for source and another one with the same configuration for the receiver. The transducers used in this experiment is 1 MHz vertical sensor. We start with the transducers on the center of the glass surface. The diameter of the transducer is 12.7 mm and we measure the distance between the two transducers as the initial offset which is about 20 mm (200 m after scaling). The computer controls the movement of the transducers and they move in the opposite direction along the survey line simulating a typical Common Midpoint Gather (CMP). At each source-receiver position, the source transducer pops 20 times (simulating vertical stack) and

the receiver transducer listens for 0.3 ms (scaled to 3 s) for each pop. The sampling rate is 0.2 us and its scaled to 2 ms which is typical for real seismic survey. The total offset is 3180 mm with 20 mm step and 150 traces. Figure 2.4 is a photo taken during the ultrasonic acquisition. Two 2D lines are surveyed and one is over fractured zone and the other off the the fractured zone for comparison.

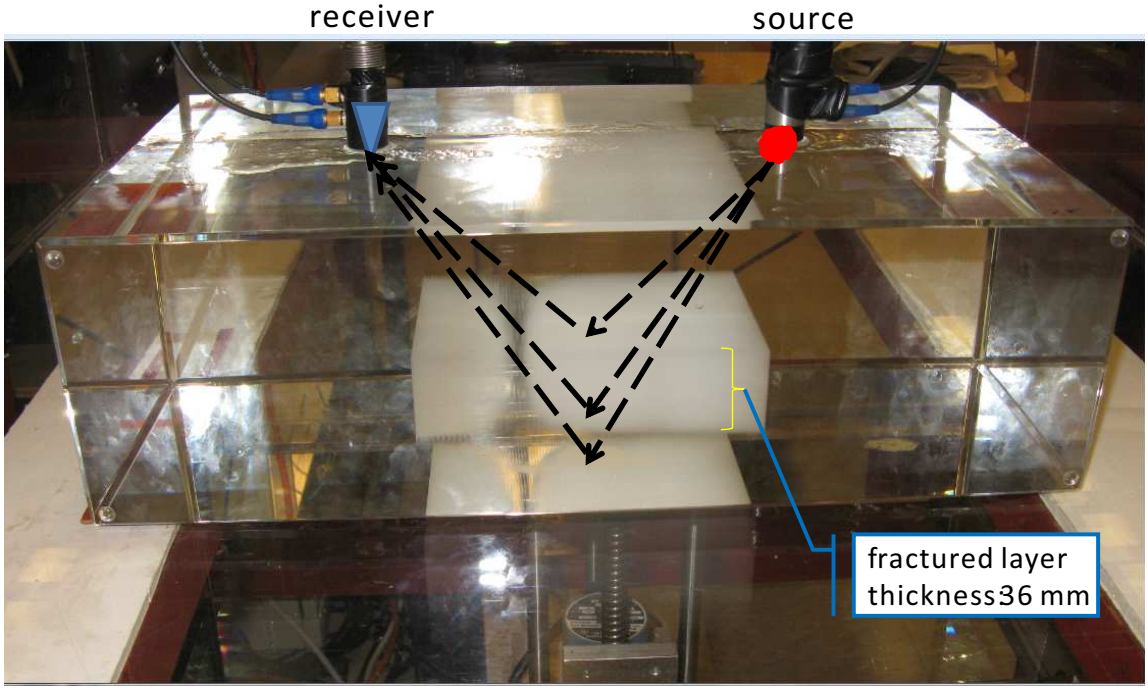

Figure 2.4: Ultrasonic acquisition system. The red marker is noted as the source transducer and the blue marker is noted as the receiver transducer. The source and receiver start from the center of the glass surface and walk away from each other simulating a CMP survey. The transducer has two component as vertical and horizontal. By simple combination of different component pair, multicomponent data could be recorded.

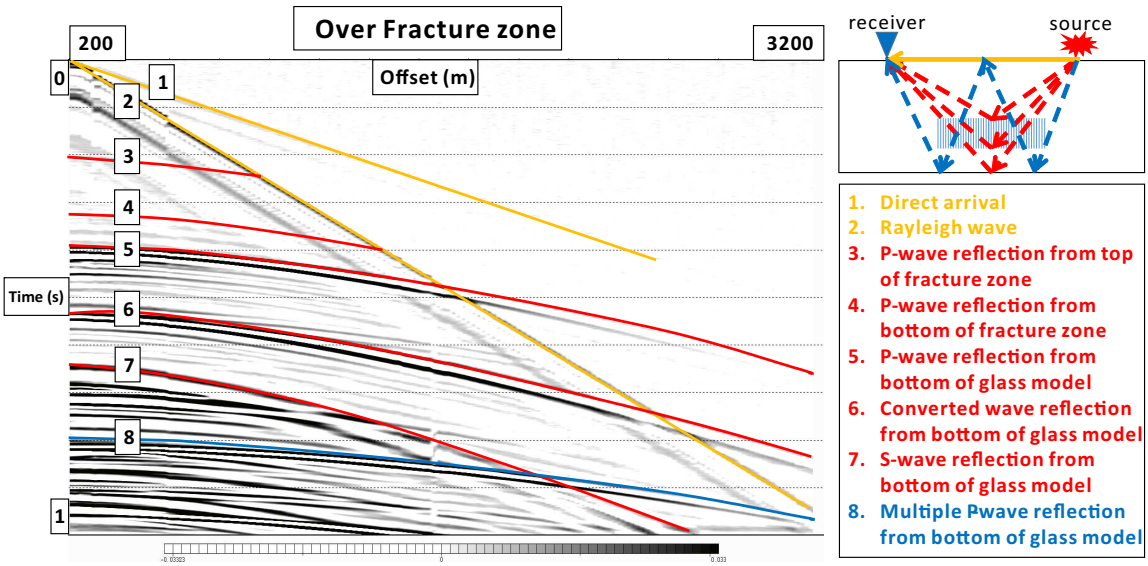

Figure 2.5: Color-coded events correlation. Yellow is coded for the waves travelling on the surface which are direct P-wave arrival (event 1) and surface Rayleigh wave (event 2). Red is coded for the primary reflections from fracture zone and bottom of the glass model. Events 3, 4, 5 are the primary P-wave reflections from the top of fracture zone, bottom of fracture zone and the bottom of the glass model, respectively. Events 6 and 7 are the primary converted wave and shear wave reflections from the bottom of the glass model. Blue is coded for the multiple P-wave reflection (event 8) from the bottom of the glass model.

Figure 2.5 is the interpretation of the data with color-coded correlation of eight major events. Yellow is coded for the waves travelling on the surface which are direct P-wave arrival (event 1) and surface Rayleigh wave (event 2). Red is coded for the primary reflections from fracture zone and bottom of the glass model. Events 3, 4, 5 are the primary P-wave reflections from the top of fracture zone, bottom of fracture zone and the bottom of the glass model, respectively. Events 6 and 7 are the primary converted wave and shear wave reflections from the bottom of the glass model. Blue is coded for the multiple P-wave reflection (event 8) from the bottom of the glass model.

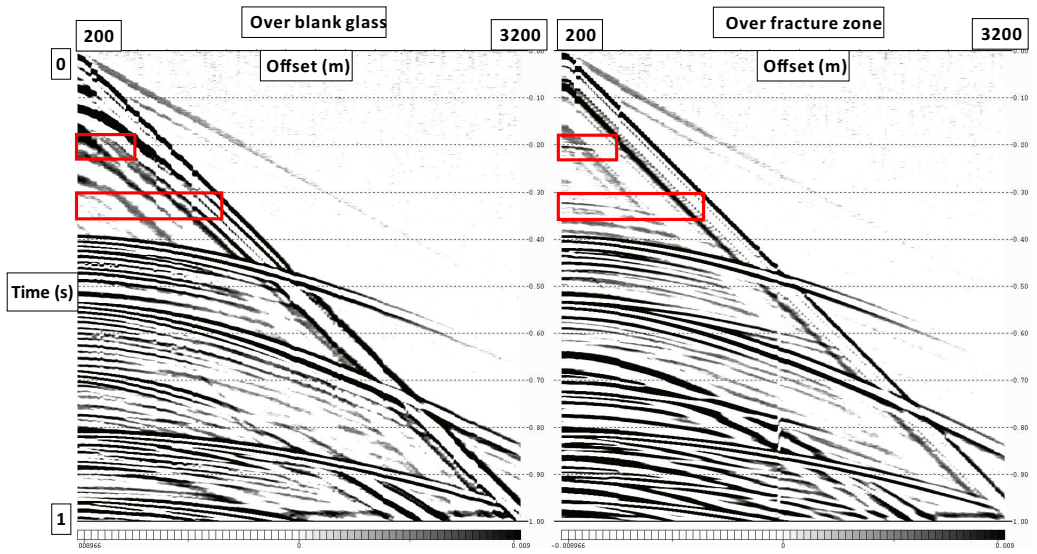

Figure 2.6: Comparison of two CMP data on and off the fracture zone. Reflections from the fracture zone is observed from the over-fracture-zone (left) CMP data while no reflections are observed from off-fracture-zone (right) survey data.

After recording the 2D line cross the fracture zone, another line which goes off the fracture zone is surveyed for comparison. By simply comparing the two survey line data, we seem to see the reflections from the fracture zones which are indicated in the red box (Figure 2.6). However, as the data are highly contaminated by the Rayleigh wave, more processing is needed to enhance the reflections from the fracture zone.

2.2.2 Multi-component surveys with different azimuth

The 2D line is surveyed with vertical sensors which records primary P-wave data but shear-wave data as well. We use horizontal sensors to see how shear waves can help us recognize fracture zone. One of the very important things is the coupling. We know that S-wave does not travel through water and usually we used honey

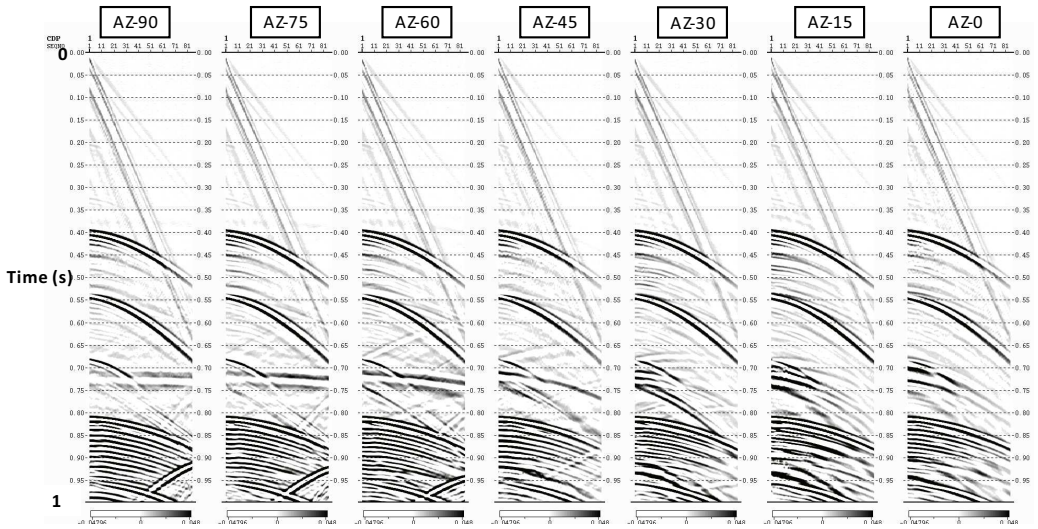

Figure 2.7: P-P data recorded from the vertical to vertical component transducer pair. Seven different azimuths from 0° to 90° are surveyed over the fracture zone.

mixed with water as the P-wave coupling medium. For S-wave, water is not friendly. So the S-wave coupling we use in the experiment is the dried honey. Since we use the computer to control the movement of transducer, the strength for pressing the transducer against the model is constant, which makes the coupling consistent during the experiment. We survey 12 2D lines with 15° azimuth increase to get 7 component azimuthal (from 0° to 360° azimuth) CMP data. These 2D lines are surveyed in the same configuration except for the total offset which is 1880 mm with 85 traces. 0° azimuth is defined as the direction parallel to the symmetry axis of the HTI fracture zone. In this case, we have P-P (Figure 2.7), P-SV (Figure 2.8), P-SH (Figure 2.9), SV-SV (Figure 2.10), SV-SH (Figure 2.11), SH-SV (Figure 2.12), SH-SH (Figure 2.13) data.

From all of the different component data, the P-P and SH-SH data are most interesting to us, as we can see the fracture reflections from raw data alone before

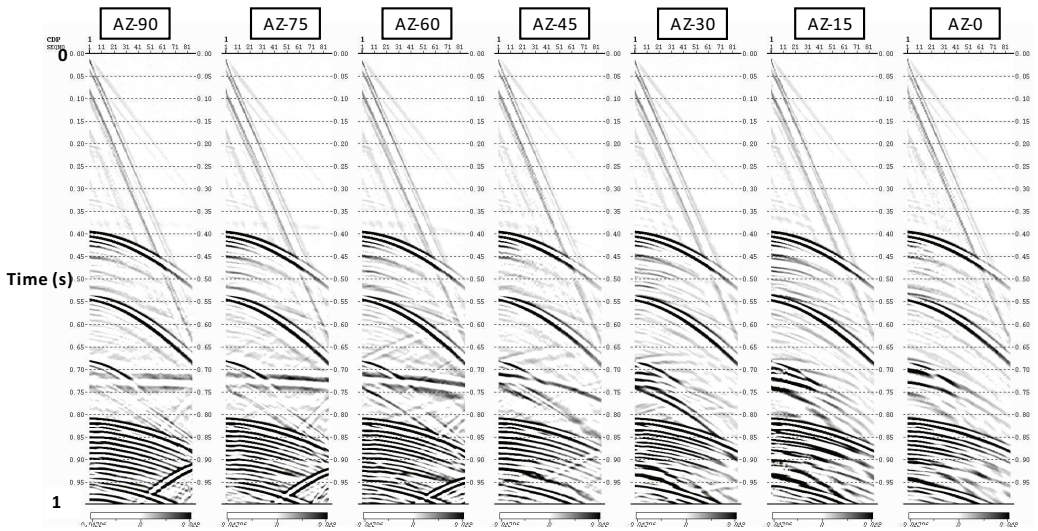

Figure 2.8: P-SV data recorded from the transducer pair of vertical to horizontal component. The horizontal component transducer is polarised parallel to survey line and is defined as a SV component. Seven different azimuths from 0° to 90° are surveyed over the fracture zone.

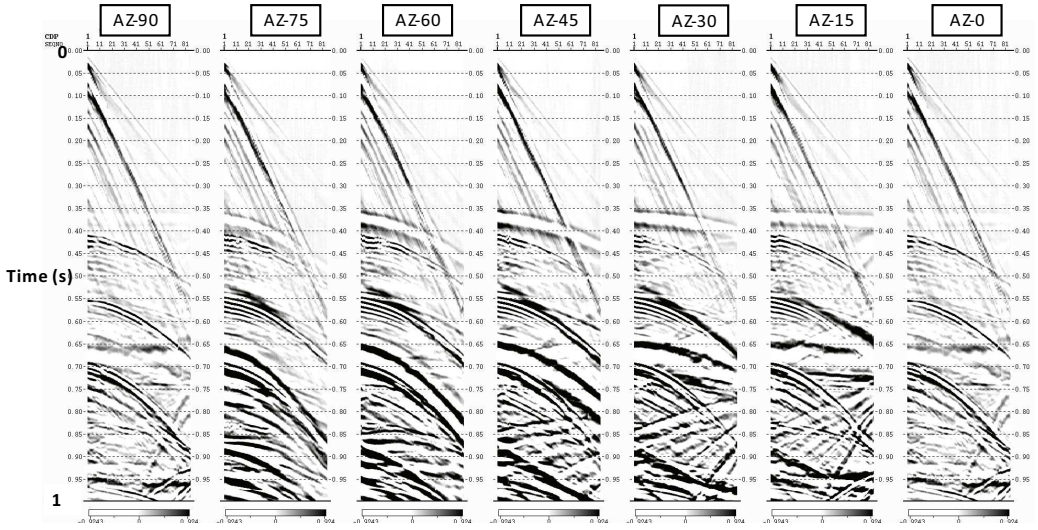

Figure 2.9: P-SH data recorded from the transducer pair of vertical to horizontal component. The horizontal component transducer is polarised normal to survey line and is defined as a SH component. Seven different azimuths from 0° to 90° are surveyed over the fracture zone.

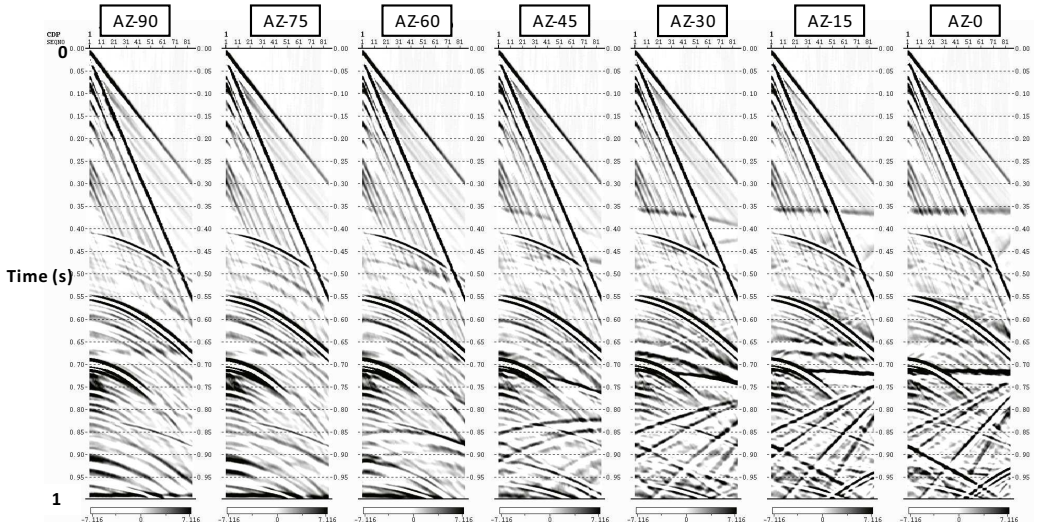

Figure 2.10: SV-SV data recorded from the horizontal to horizontal component transducer pair. Both horizontal component transducers are polarised parallel to survey line and thus defined as a SV component. Seven different azimuths from 0° to 90° are surveyed over the fracture zone.

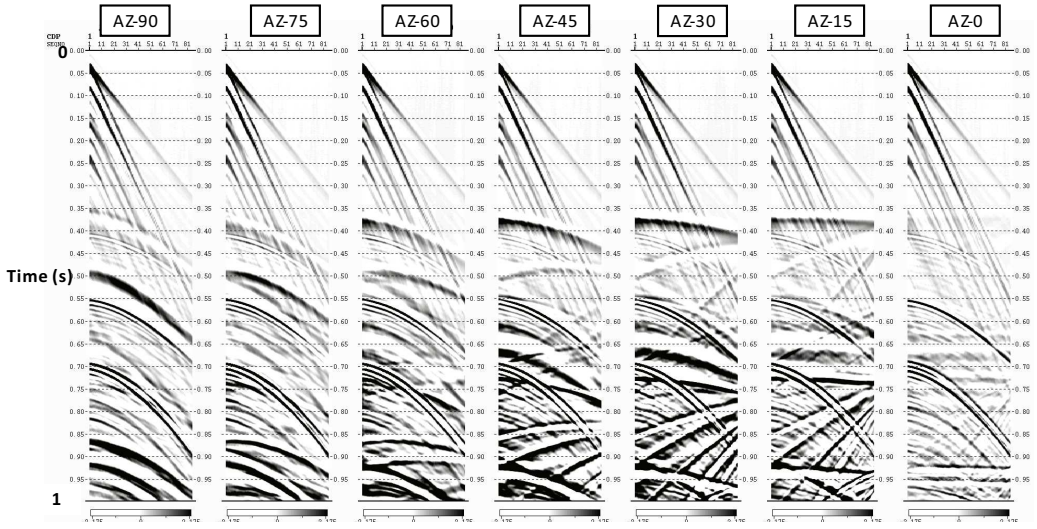

Figure 2.11: SV-SH data recorded from the horizontal to horizontal component transducer pair. The source horizontal component transducer is polarised parallel to survey line and thus defined as a SV component. The receiver horizontal component transducer is polarised normal to survey line and thus defined as a SH component. Seven different azimuths from 0° to 90° are surveyed over the fracture zone.

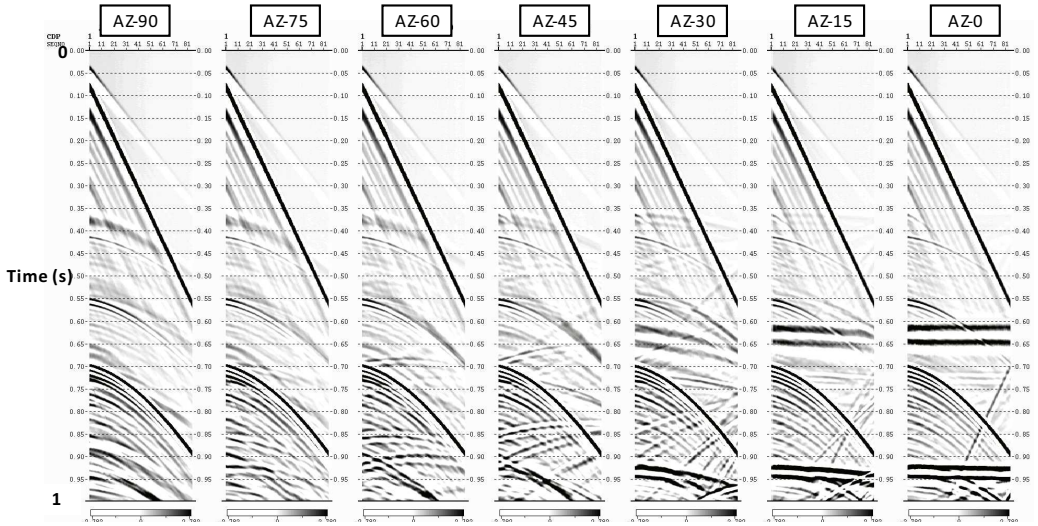

Figure 2.12: SH-SH data recorded from the horizontal to horizontal component transducer pair. Both horizontal component transducers are polarised normal to survey line and thus defined as a SH component. Seven different azimuths from 0° to 90° are surveyed over the fracture zone.

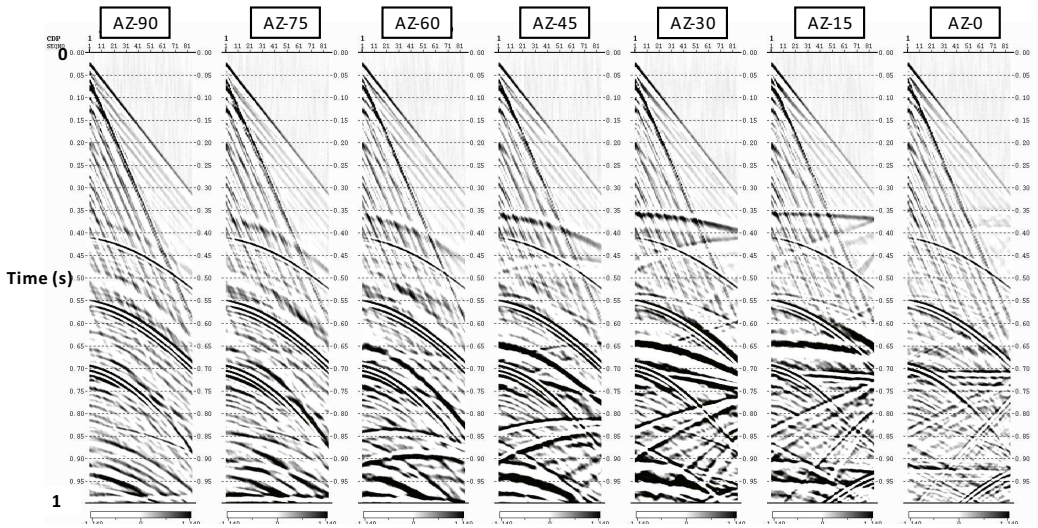

Figure 2.13: SH-SV data recorded from the horizontal to horizontal component transducer pair. The source horizontal component transducer is polarised normal to survey line and thus defined as a SH component. The receiver horizontal component transducer is polarised parallel to survey line and thus defined as a SV component. Seven different azimuths from 0° to 90° are surveyed over the fracture zone.

processing. In this case, we decide to process these two data sets to see if we can get some information about the fracture zone. An AVO (Amplitude Versus Offset) or AVAZ (Amplitude Versus Azimuth) analysis is performed to invert for fracture orientation. Before doing this analysis, a correction for directivity is needed.

2.3 Data processing and analysis

2.3.1 Data processing to enhance fracture zone reflections

We process the data to enhance the fracture zone reflections by removing the Rayleigh wave and attenuating noise. Figure 2.14 is the workflow for data processing. First, the data are recorded with the ultrasonic system and converted into segy file with geometry. Then we input the data into processing software (Echos and VISTA were used). First, to remove the Rayleigh wave, a FK filter is used (Figure 2.15) to remove most of the Rayleigh wave which contaminated the data. Then velocity analysis is applied and P-wave velocities are picked and used in the NMO correction to flatten all the P-wave events (Figure 2.16). Since all the P-wave events are flattened, a median filter (Figure 2.17) can preserve the P-wave events and remove all other events and noise to enhance the P-wave reflections from the fracture zone. The length of the median filter used here is seven point. After all the processing flows are done, we are able to see the reflections from the fracture zone more clearly as showed in Figure 2.14.

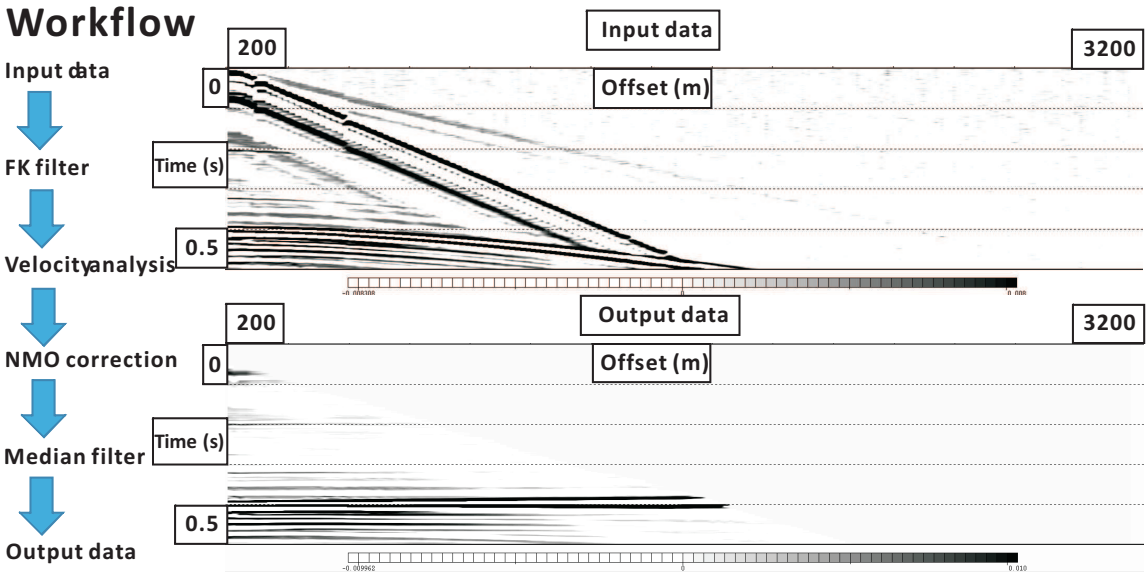

Figure 2.14: Workflow for data processing to remove noise and enhance the fracture zone reflected signals. The target signals are flattened and filtered with median filter.

2.3.2 Transducer signature study for AVO/AVAZ analysis

In order to correct for the directivity or radiation pattern of the source and receiver. a study of the transducer signature is performed. The transducers in Allied Geophysical Laboratories (AGL) have different central frequency, bandwidth, radiation pattern and waveform. It is very important to understand their signatures as source or receiver. For example, the central frequency for different transducer is always smaller than the manufacturer's instruction. However, it's important to know its true central frequency for the calculation of wavelength.

The transducers used for ultrasonic experiments are piezoelectric transducers. These kinds of transducers use the piezoelectric effect of the crystals which generates a voltage when deformed. It actually converts mechanical movements (vibration)

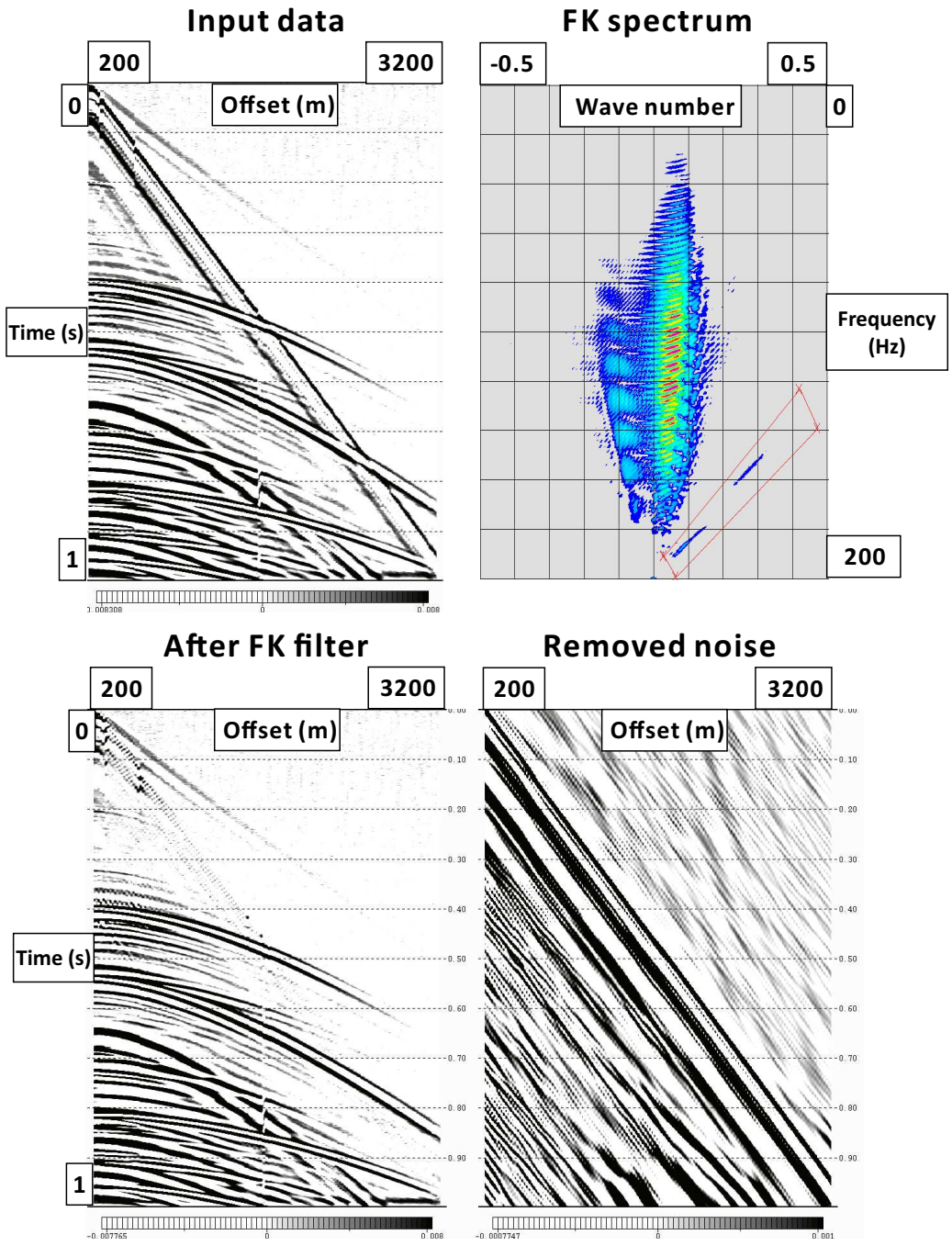

Figure 2.15: A polygon FK filter is defined as marked in red. After this FK filter, most of the Rayleigh wave which contaminates the fracture zone reflections is removed.

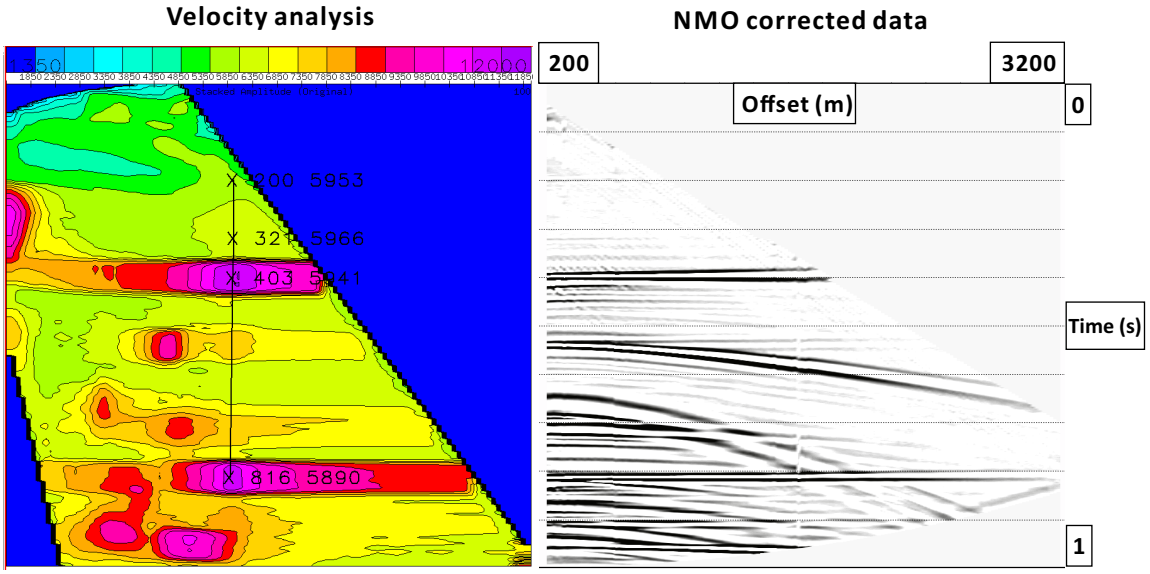

Figure 2.16: Velocity analysis and NMO corrected data with the picked P-wave velocities. After this processing, all the P-wave events are flattened.

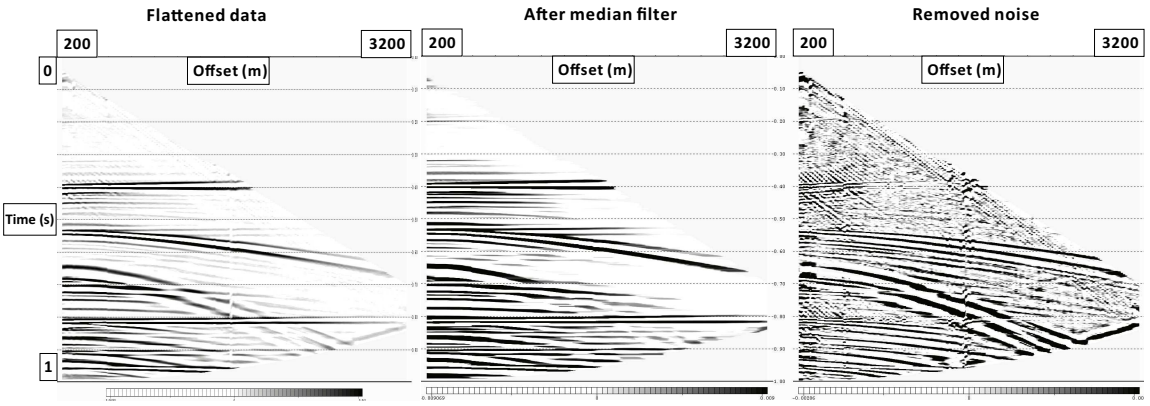

Figure 2.17: A seven point median filter is applied to filter unflattened events and fracture zone reflections are enhanced through this processing.

to and from electric signal. In our experiments, we send an electric signal to the transducer and it vibrates. Next the vibration or wave transmits through the front plate of transducer to the model and then to the other transducer which acts as a receiver.

The waveform from the transducers are not the same with what we have in the field. Field data usually have stable waveforms from a few kinds of impulsive seismic sources, which are explosives, air gun, vibroseis, etc. These seismic sources generate impulsive signals which are usually zero phase wavelet. Ultrasonic sources, however, theoretically generates waves which is the first derivative of the input electric signal sent to the transducers. For example, if we sent a sine signal to the transducer as a trigger, we will get a cosine wave as output. The trigger we used in our experiments is the Olympus Pulser-receiver, Model 7077PR. This pulser-receiver can provide square excitation to trigger a transducer. Pulser-receivers employed with ultrasonic transducers and an analog or digital oscilloscope, are the prime building blocks of any ultrasonic test system. The pulser section produces an electrical pulse to excite a transducer that converts the electrical input to mechanical energy, creating an ultrasonic wave. In pulse-echo applications, ultrasound travels through the test material until it is reflected from an interface back to the transducer. In transmission applications, the ultrasound travels through the material to a second transducer acting as a receiver.

In our experiments for investigating the waveforms generated from our transducers, we tested square excitation with different pulse width to compare and select the best waveform we want and modify the central frequency of different transducers at the

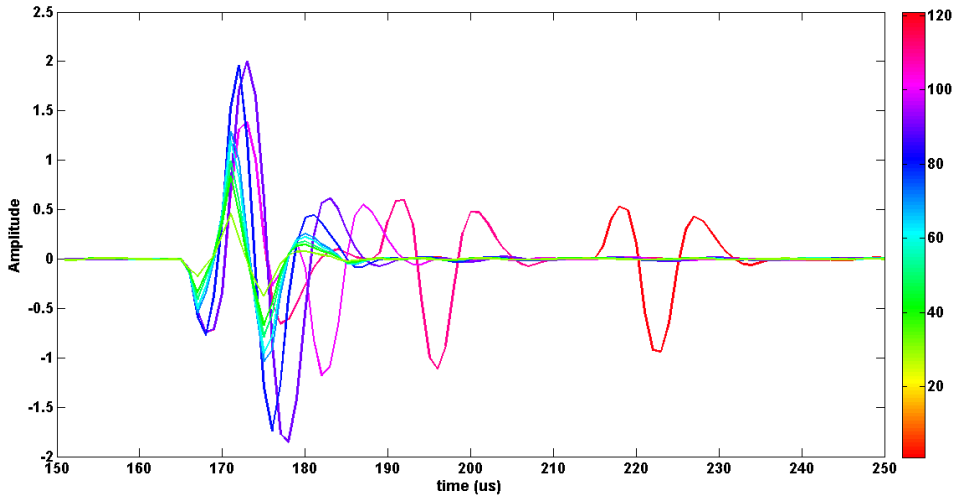

Figure 2.18: Waveform change with different different pulse width excitations. The best waveform appears when the pulse width is closer to transducer central frequency.

same time. We put transducers in the center of two opposite surfaces and record each time with ten different pulse widths ranging from 100 kHz to 20 MHz.

In Figure 2.18, we can see the different waveforms driven by different pulse widths. The color bar here shows different square wave frequency or pulse width. We can see that the increase or decrease of square wave signal generates an impulse response, so for a square wave excitation, we have two impulse signals and they have opposite polarity. If we decrease the pulse width, the two impulse waves will be added together so that we see the waveform have two peaks and troughs. However, as for the amplitude of the waveform, it is strongest when the square wave frequency is most close to the transducer's central frequency. Besides amplitude factor, frequency spectrum is also an indicator for pulse width selection. For example, for a 1 MHz transducer, if we input a 100 kHz square wave for excitation, we will end up with

ten notches in its frequency spectrum which is definitely not what we want. From the waveform measurement, we can easily get the transducer central frequency. For the 1 MHz transducer which we use in our experiments, its actual central frequency is 0.95 MHz.

Normally we investigate the radiation pattern by making one transducer as the source and another one as receiver. We stable the source and rotate the receiver in a single plane with constant offset and see how the amplitude changes with different angles. This requires a system that can precisely control the angle of rotation which is very important for the measurements. However, we do not have such facilities in our lab to satisfy the requirements and thus we have to do it in another way. We make a transmission survey. We may have a problem for making the source and receiver at the exact opposite position through the glass block. However, we know that radiation pattern should be generally symmetric and the maximum amplitude should be at the zero-angle position. So we can simply run the experiments making the source in the more or less center of the bottom of the glass block and mover the receiver at the top surface. We try our best to make sure the receiver run across the line in the center of the top surface and measure its initial position. Then we use our computer to control the movement of receiver to move from one side to the other. The total length of the survey line is 180 mm and every step is 1 mm. We record the data at each step point and the data as a whole actually become a seismogram. Remember that the data are from a transmission survey through a blank glass. In this case, the first arrival we record here seems to have some AVO response but this is only the result of the radiation pattern of transducer. So if we pick the maximum amplitude

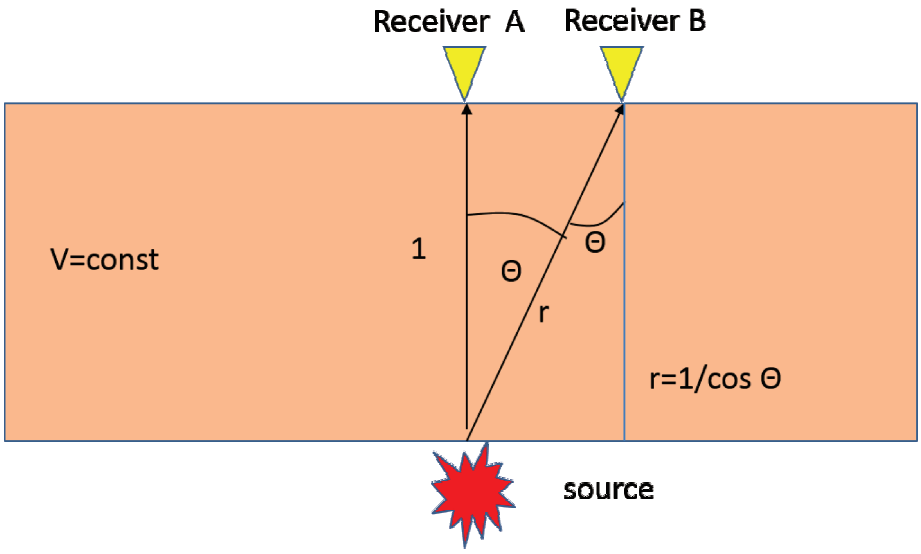

Figure 2.19: Schematic for the derivation of radiation pattern. The red and yellow markers denote the source and receiver transducers respectively.

of the first arrival of each trace, we can simply know how amplitude changes with offset as a result of directivity. As we know the height of the glass, we can calculate the incidence angle for each offset thus we get how amplitude changes with directions which is the radiation pattern or directivity we want. However, there is one more thing we need to take care of. The length of each ray from different angle of incidence is different and the transducers acting as receivers are not heading directly to the source transducer which means we are having the effect of double radiation pattern. To correct for length difference and double radiation pattern, we can simply derive the relationship between radiation pattern and the amplitude change with angle.

As we can see in Figure 2.19, if we assume $\boldsymbol{R(\theta)}$ is the radiation pattern of the transducer, the height of the glass is assumed to be 1, $\boldsymbol{\theta}$ is the incidence angle, r is the ray length or the traveling distance, then $\boldsymbol{r = 1/\cos(\theta)}$. Imagine the source

generates a wave, when it travels to a point, the amplitude should be $\boldsymbol{R(\theta)/r}$, then we have a receiver at the point to receive the wave energy. If the receiver receives the wave at the point shown as Point A, then it can receives the all the energy which we define as 1. However, when it comes to some other point like Point B, the receiver has the same radiation pattern but we don't have the problem for distance correction. So at any point, the signal we recorded $\boldsymbol{F(\theta)}$ is the combination of both the source and receiver. And it's

$$\boldsymbol{F(\theta) = [R(\theta)/r]R(\theta), r = 1/\cos(\theta),} \tag{2.7}$$

so

$$\boldsymbol{F(\theta) = [R(\theta)\cos(\theta)]R(\theta) = R(\theta)^2\cos(\theta),} \tag{2.8}$$

or

$$\boldsymbol{R(\theta) = F(\theta)/\sqrt{\cos(\theta)},} \tag{2.9}$$

This is the correction from which we can get the correct measured radiation pattern. So after running the experiments, processing the data and making the corrections, we finally got the radiation pattern show as in Figure 2.20. We study all different kinds of transducers. We can see from the figure that a lower frequency transducer has a broader radiation pattern which can record data with longer offsets; whereas a higher frequency transducer has a narrower radiation pattern which limits the offsets we can record. The conclusion we got agrees with our general understanding of directivity. To correct for the specific data we record with the 1 MHz vertical component transducer, more corrections are made. Buddensiek et al. (2009) study

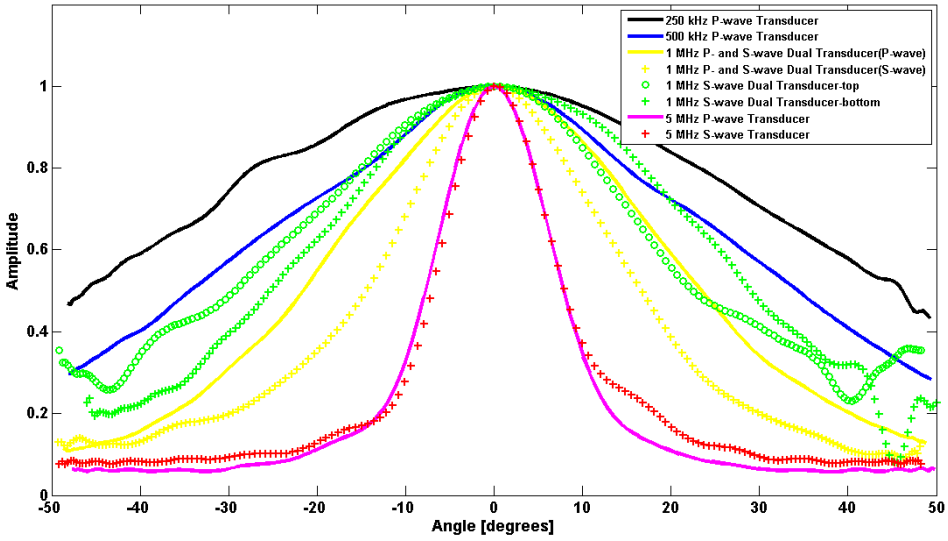

Figure 2.20: Radiation pattern recorded with 6 different transducers. Note that the higher the transducer frequency, the narrower the frequency band.

the transducers in detail and give the equations for directivity (Equations 2.10 and 2.11).

$$p(p_0, D, \lambda, z, \gamma) = 4p_0 \frac{J_1(X)}{X} sin(\frac{\pi D}{8\lambda z}) \tag{2.10}$$

with

$$X = \frac{\pi D}{\lambda} sin(\gamma) \tag{2.11}$$

where p_0 is the initial pressure (amplitude), D is the diameter of the emitter, λ is the wavelength, z is the distance to the emitting plane, γ is the incidence angle, and $J_0(X)$ is the first kind Bessel function. For the transducer we use in our experiment, D= 12.7 mm, λ= 5.8 mm, z= 79 mm. With these known parameters, we can plot directivity as a function of incidence angle and fit the equation with

unknown initial pressure $\boldsymbol{p_0}$ to measured directivity curve (Figure 2.21). With the theory fit directivity, we can use it to correct for amplitude in AVO/AVAZ analysis.

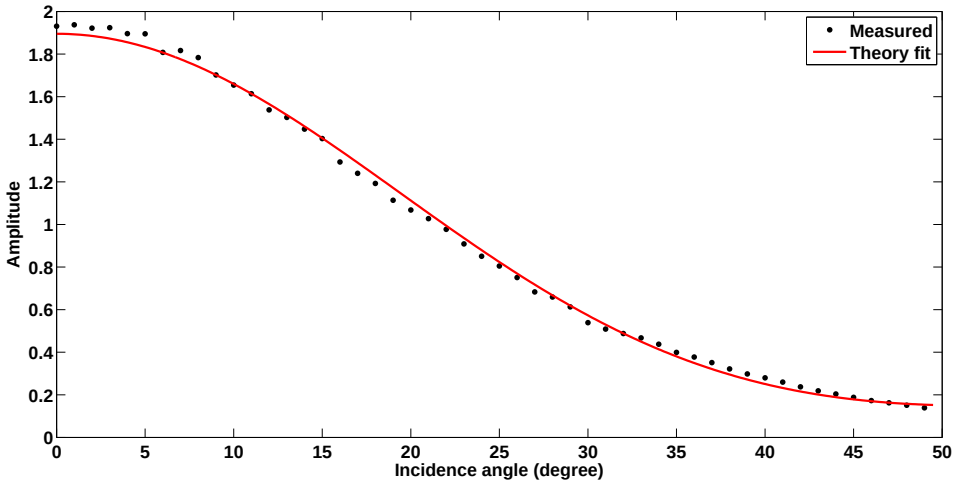

Figure 2.21: Directivity fit with measured data. The dots are measured amplitude at each incidence angle and the red curve is the theoretical curve fit to the data.

2.3.3 AVO/AVAZ analysis

The very same processing flows are performed on the azimuthal P-P data and we get the median filtered flattened data shown in Figure2.22. The reflection from the bottom of the fracture zone comes around 320 ms. From velocity analysis, we are not able to see any azimuthal change in terms of NMO velocity because the azimuthal velocity is very subtle. However, if we look at the AVO curve change with azimuth, we are able to tell the difference in terms of azimuth (Figure 2.23). By calculating the incidence angle from offset and depth, the incidence angle varies from 6° to 35°. However, the data from 25° to 35° are highly contaminated with the noise making the

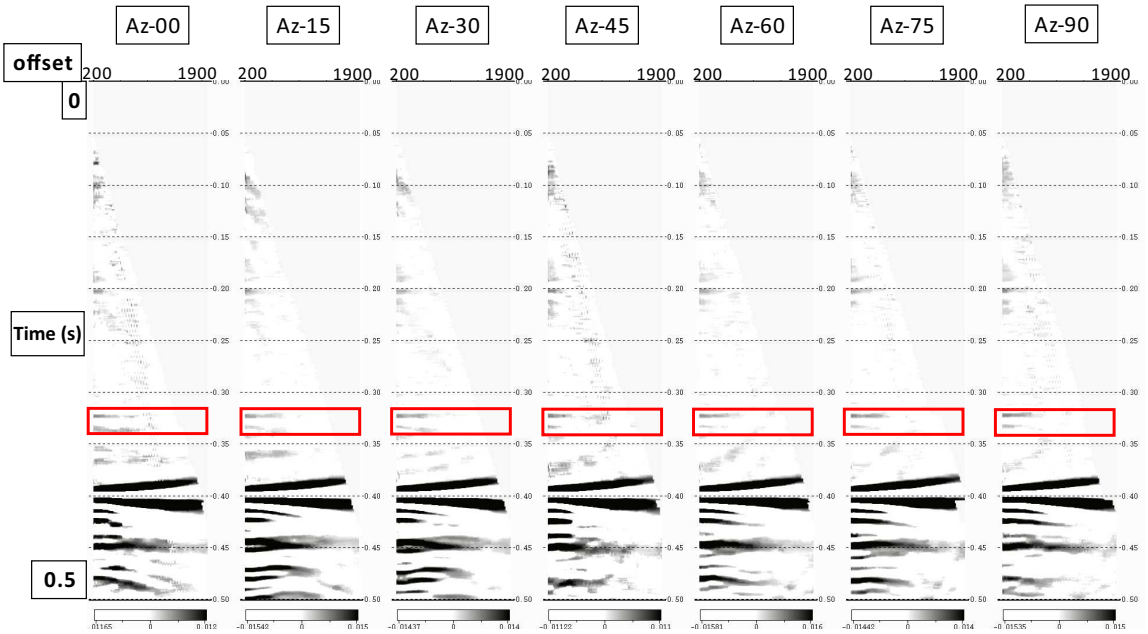

Figure 2.22: Median filtered flattened azimuthal CMP data (vertical to vertical component.)

AVO curve going crazy, so this part of data is abandoned. The reflection coefficient for P-P reflection is given by Rüger (2001).

$$
\begin{aligned}
R_{PP}(\theta,\phi) = & \frac{1}{2}\frac{\Delta Z}{Z} + \frac{1}{2}\{\frac{\Delta V_{PO}}{V_{PO}} - (\frac{2V_{S0}}{V_{P0}})^2\frac{\Delta G}{G} \\
& + [\Delta\delta^V + 2(\frac{2V_{S0}}{V_{P0}})^2\Delta\gamma]cos^2\phi\}sin^2\theta \\
& + \frac{1}{2}\{\frac{\Delta V_{PO}}{V_{PO}} + \Delta\epsilon^V cos^4\phi + \Delta\delta^V sin^2\phi cos^2\phi\}tan^2\theta sin^2\theta
\end{aligned}
\tag{2.12}
$$

We can clearly see the change in the trend of the AVO curve with different azimuth. Azimuth 0° which is direction normal to the fracture planes has the biggest curvature while azimuth 90° which is parallel to the fracture planes has the smallest curvature.

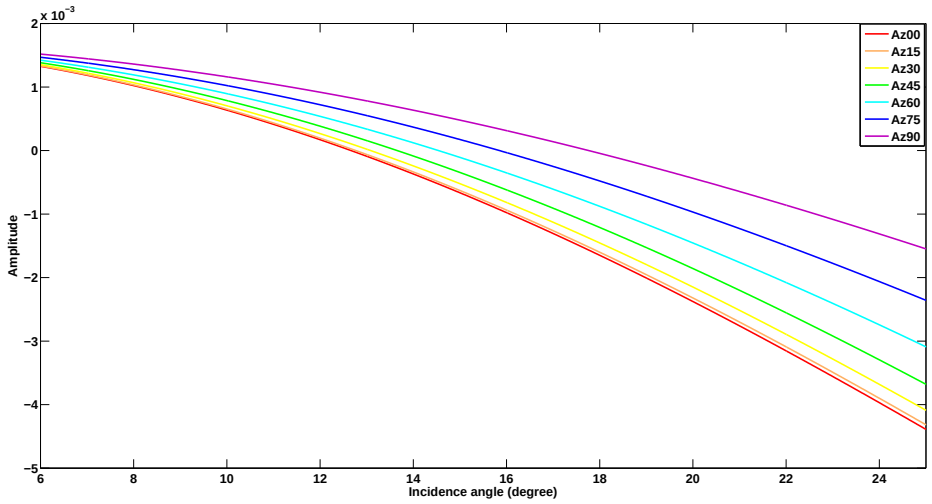

Figure 2.23: AVO change with azimuth. The azimuth is color coded with the color sequence of rainbow from 0° to 90° with 15° increment.

From the processed data, we can simply extract the amplitudes of the reflection from the bottom of the fracture zone. By converting the offset into incidence angle, we can make angle stack for every one degree then plot the curve as amplitude versus incidence angle (Figure 2.24). There seems to be some trend which tells us about the azimuthal difference. To invert for the azimuth, we use Equation 2.12 to fit the measured AVO with unknown azimuth. The different azimuth fit gives different R square (coefficient of determination value) for the fit of measured data. The azimuth which gives the highest R square value is considered as the right azimuth for that data. Take the 0° azimuth data for example (Figure 2.25), we plot the R-square versus azimuth and find that the 0-azimuth which is the right azimuth fits the data best. Thus, we determine the azimuth of the data. The same procedure is done for different azimuth data and their azimuth is inverted. However, not all data has good enough S/N (signal to noise ratio) to make the fitting method work. But in general,

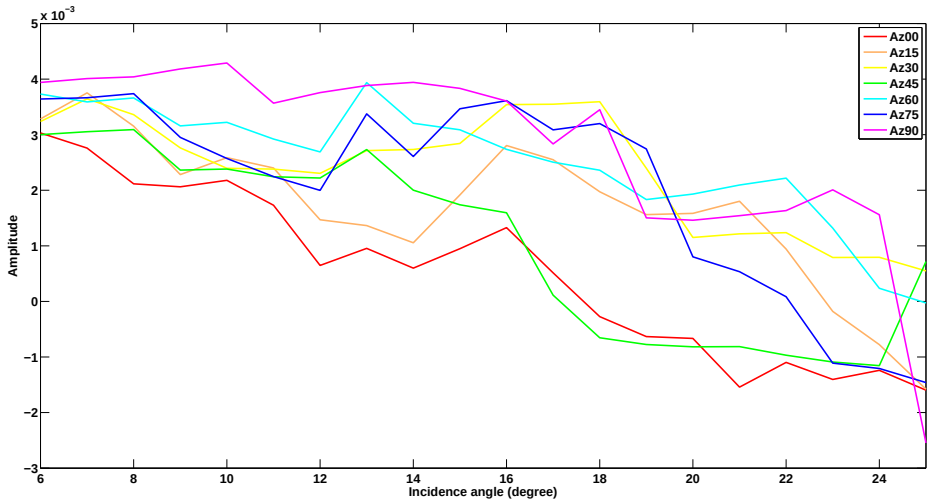

Figure 2.24: Measured AVO change with azimuth. The azimuth is color coded with the color sequence of rainbow from 0° to 90° with 15° increment.

we are able to get the azimuth from good data.

Azimuthal stack of amplitude is also done to invert for azimuth. Figure 2.26 shows the stacked azimuthal amplitude versus azimuth. The curve follows a trend as stacked amplitude increases with azimuth which agrees with theory. However, these data points can give two different trends as one is lined with azimuth 0°, 15°, 30°, 60°, and 90°, and the other with 0°, 45°, 75°, and 90°. This may be caused by the data quality and noise level. Remember the reflected signal is quite weak compared to background noise. If the data quality is bad, this method for inverting azimuth would crash. In this case as we study, the stacked amplitude should increase slowly at first then fast which agrees withe trend from azimuth 0°, 45°, 75°, and 90°. Thus, the data from azimuth 15°, 30°, and 60° may have some problems causing their abnormal high amplitude.

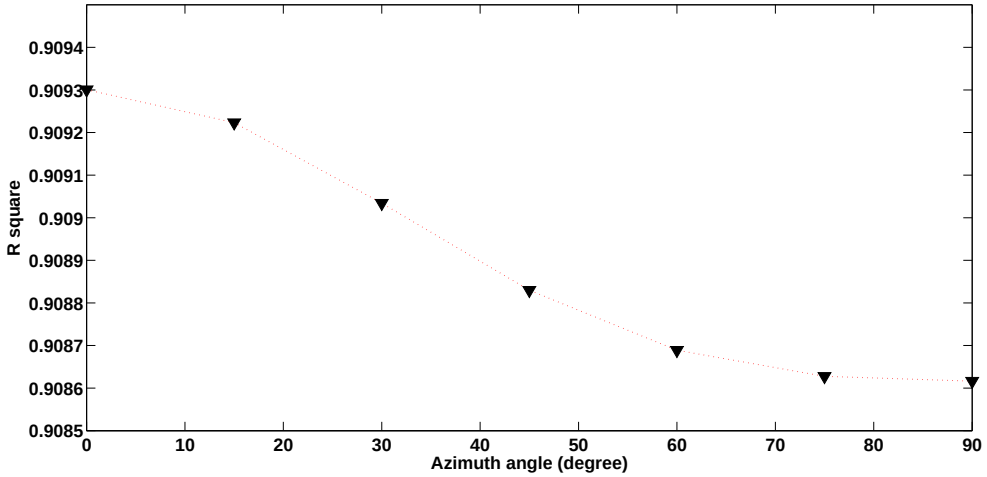

Figure 2.25: R square versus azimuth to invert for the right azimuth. The triangle marker is noted for the R square value for different azimuth and a clear trend is observed.

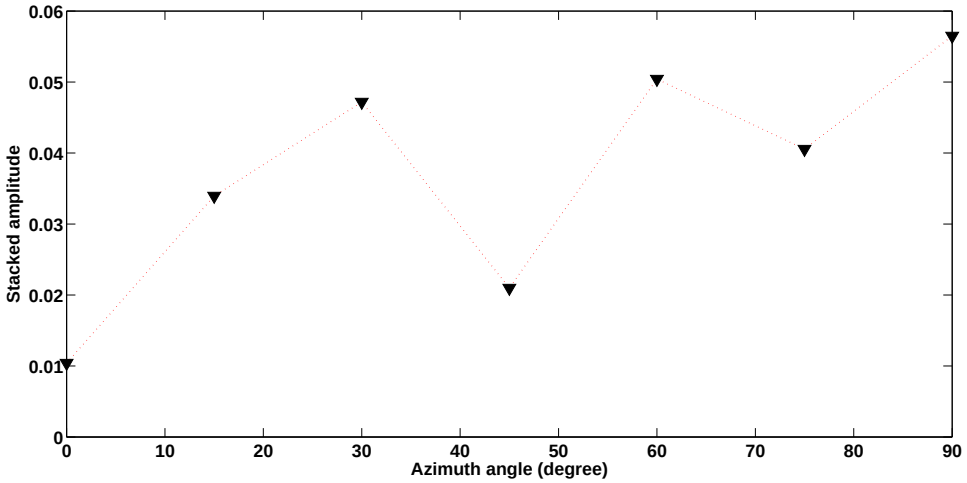

Figure 2.26: Azimuthal amplitude stack. The amplitude is stacked for each azimuth and there seem to be two different trends for the stacked amplitude variation with azimuth.

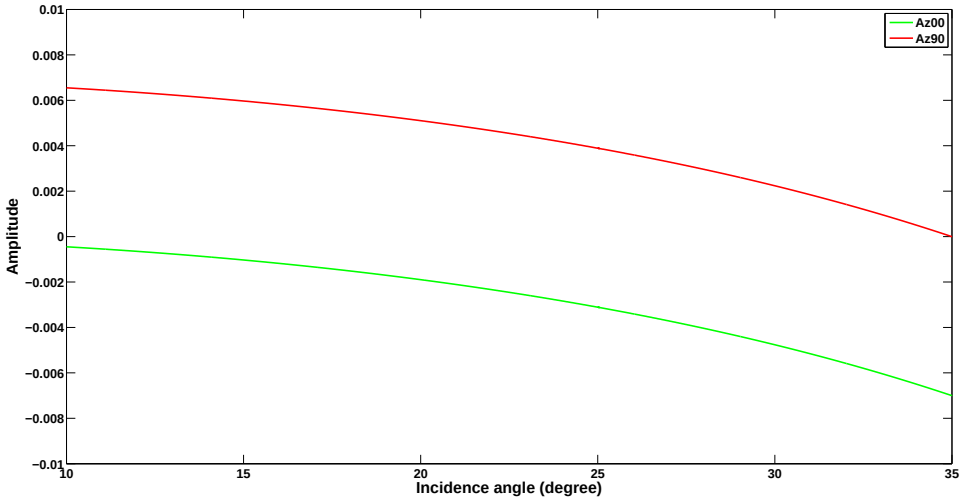

Figure 2.27: AVO curve for azimuth 0° and 90° of the SH-SH component.

For the SH-SH data, the same processing flows are performed but with shear wave velocity used to NMO correct the data instead of P-wave velocity. The shear wave (polarized in crossline direction) amplitude change is more obvious than P-wave (Figure 2.27). We can find that in azimuth 90°, the survey line is parallel to the fracture plane but the shear wave is polarized normal to the fracture plane. The reflected shear wave amplitude is 41 times stronger than the reflected amplitude from azimuth 0°. In this way, we expect to see the amplitude of the reflected shear waves increases with azimuth from 0° to 90°. In 0° azimuth, we expect to see very weak, if any, reflections. Figure 2.28 shows the processed data. The flattened events in the red box is the shear wave reflection from the top of the fracture zone. As expected, the reflection becomes stronger with increasing azimuth. It is directly visible to tell the right azimuth without further AVO analysis. We try to follow the same procedures as we do for the P-wave data, to quantitatively interpret the shear

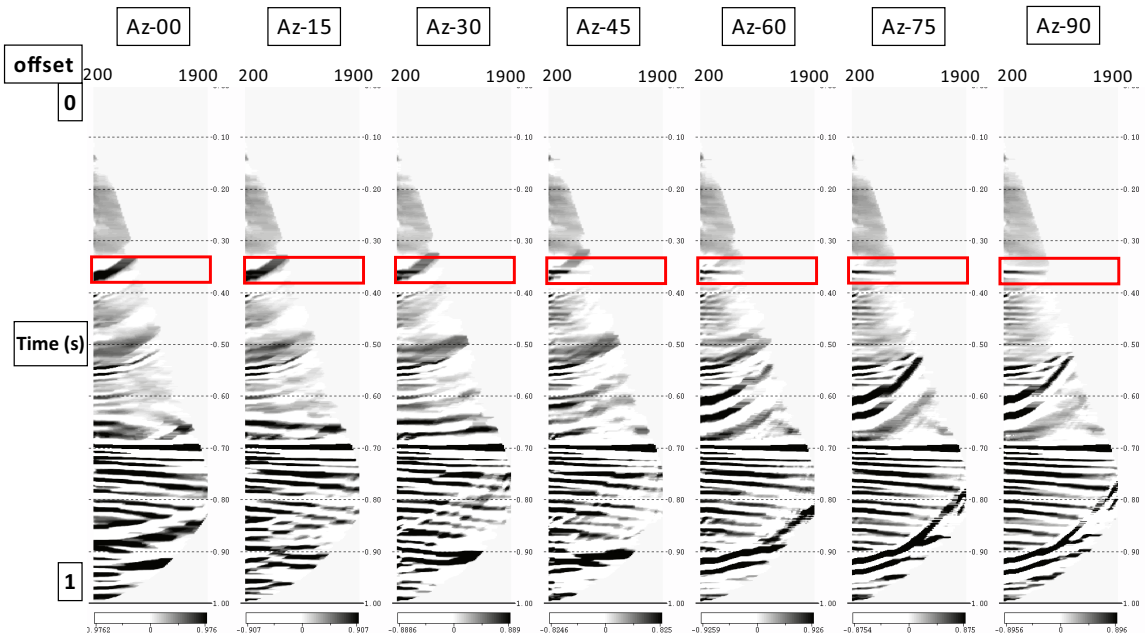

Figure 2.28: Median-filtered, flattened azimuthal CMP data (SH-SH component). The red box highlight the shear wave reflections from the top fracture zone interface. The reflected signal decrease rapidly from azimuth 90° to azimuth 0° and the signal is highly contaminated by noise.

wave data. However, there is almost no reflected signals from the fracture zone in azimuth 0°, 15°, and 30°. In this case, if we pick the amplitude from the same time, we are picking only noise. As showed in Figure 2.29, the amplitude change with incidence angle for different azimuth has no trend to follow because as the reflections become weaker, the noise becomes dominant. In the presence of strong noise, we can not perform the same AVO analysis as we do for the P-wave data. The same problem repeats for the other component datasets and we will not further discuss them.

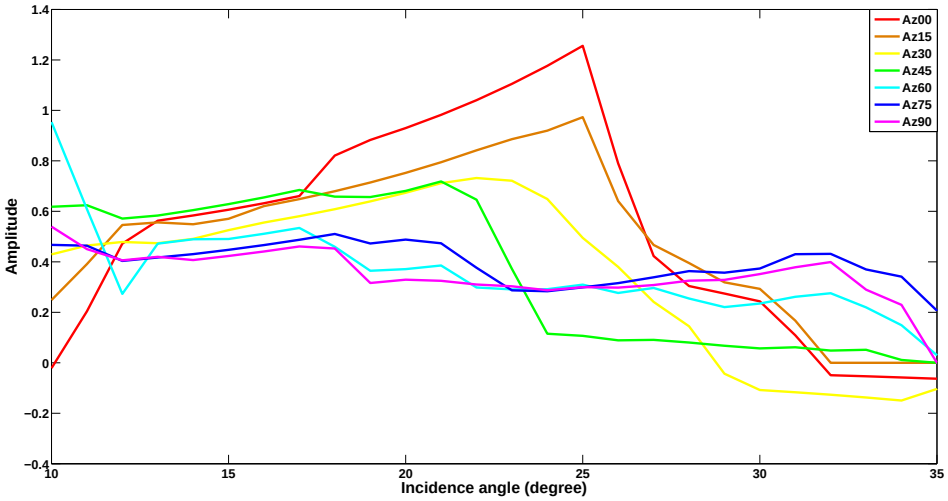

Figure 2.29: Measured AVO change with azimuth. The azimuth is color coded with the color sequence of rainbow from 0° to 90° with 15° increment. The AVO curves are rather random because the signal is highly contaminated by noise.

2.4 Discussion

The initial idea for designing this glass model is to record both P-wave and converted wave reflections from the fracture zone and joint invert the fracture parameters using AVO analysis. Now, we are able to get P-wave reflections from the fracture zone, but not converted wave reflections. Even though we have the P-wave reflections from the fracture zone, it is still difficult to do AVO inversion because the elastic property contrast between fracture zone and blank glass is too weak. Also, unexpected events come in the way to mix with desired events making it even more difficult to get the true amplitude.

Here is a brief summary of problems with this glass model.

1. Laser-etched fracture intensity. The previous glass models which are used to investigate scattering imaging have two different kinds of fractures (Figure 2.30). One is a mild fracture with small laser-melt dots and they connect one by one to create fine point clouds; the other is big crack created by intense cracking. Their difference is obvious. With mild cracking, we can create fracture planes with very small spacing while intense cracking will create stronger resistance for wave to travel, which means we will have bigger velocity difference and stronger anisotropy. When we design this new glass model, we want to create intensive cracks with small spacing (0.5 mm) so that we will have big enough wavelength-to-spacing ratio to work under effective medium domain and strong impedance contrast between glass and fractures so that we will receive strong reflections. However, the model is ordered and manufactured by a company who does not fully understand what we want from the glass. It turns out to be a glass block with mild fracturing making the fractured zone not so much fractured as we expected. In this case, the model fails our initial design.

2. Glass dimension. Usually physical models are quite big so that reflections from boundaries would come late enough not to mix with expected signals. However, as the glass is very expensive and limited by its dimension, such artifacts cause all kinds of boundary reflections. For example in Figure 2.31, the flat events (highlighted in yellow) coming around 0.7 s are the Rayleigh wave reflected back from the glass boundary as showed. Simple calculation can prove this is the Rayleigh wave side reflections. On one hand, the central frequency of this event is about 40 Hz which matches the Rayleigh wave. On the other hand, by

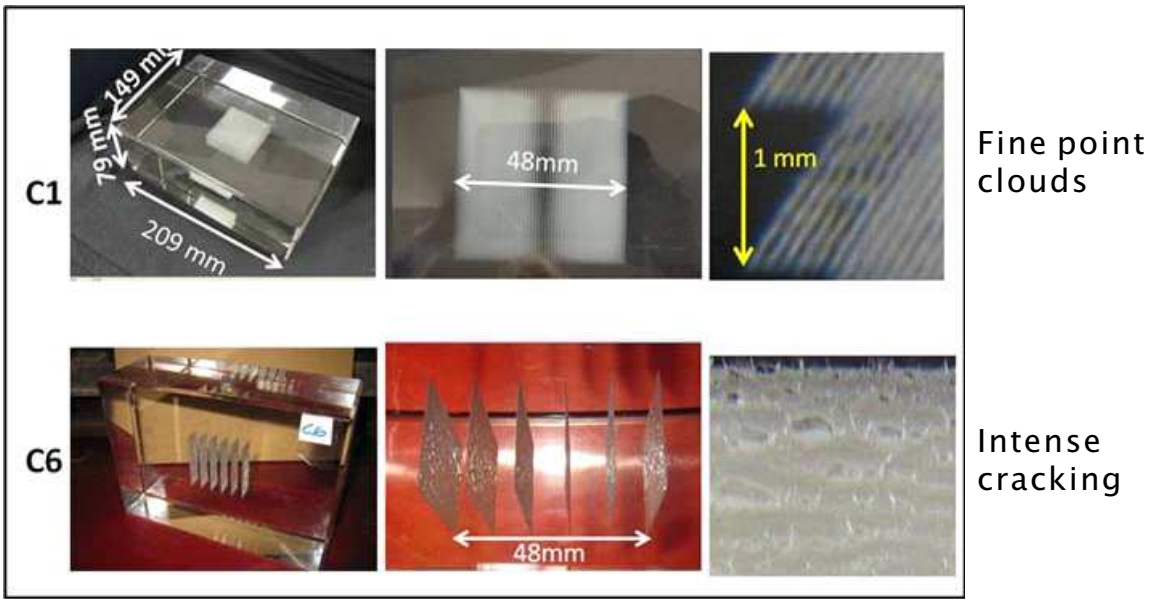

Figure 2.30: Two sets of fractures described as fine point clouds and intense cracking.(Courtesy of Robert Stewart)

travel time inversion, we can calculate the velocity of this event. The result is about 3100 m/s and also matches with Rayleigh wave velocity which is about 0.91 times shear wave velocity. Such side reflections are not limited to Rayleigh wave only. We also see side reflected P- and S-waves from different data. For example, in Figure 2.32 there is a event coming around 0.38s with a NMO velocity of P-wave. This is interesting as its moveout change with azimuth. The model edge acts as a reflector, not in depth but on surface. Even worse, the time arrival of this event is embarrassing because it comes almost at the same time as the fracture zone reflections.

3. Transducer limit. Another problem with this ultrasonic physical modeling survey is that the transducer has some limitations. On one hand, the size of the transducer is usually in centimeters and it's about hundreds of meters after

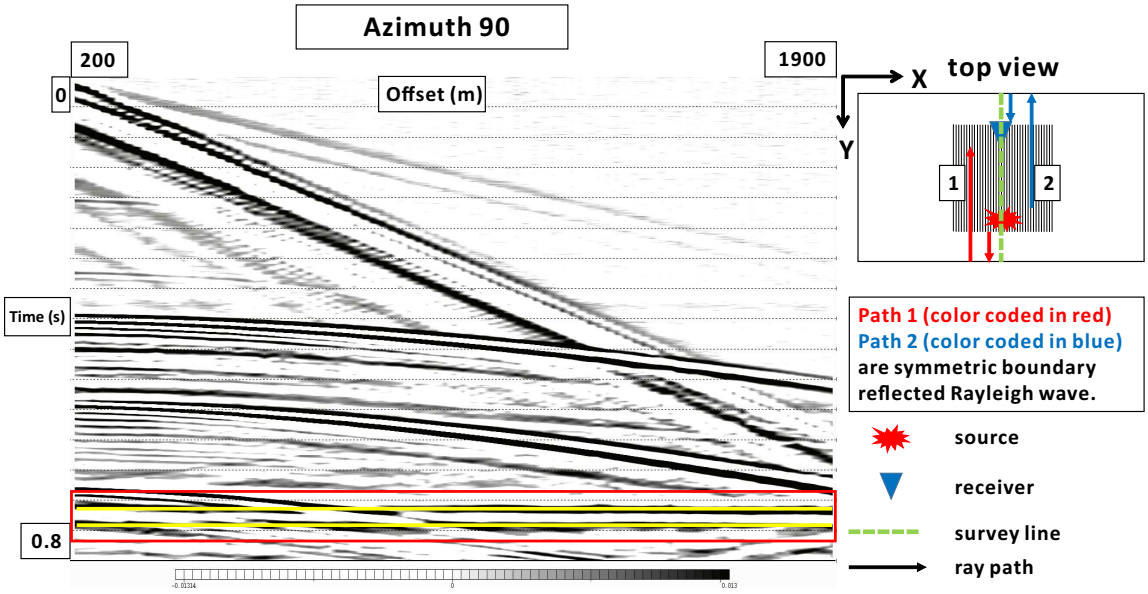

Figure 2.31: An example of boundary reflected Rayleigh wave. The red box and yellow events highlighted in the data show the boundary reflected Rayleigh wave while on the right is the schematic of the ray path for this events.

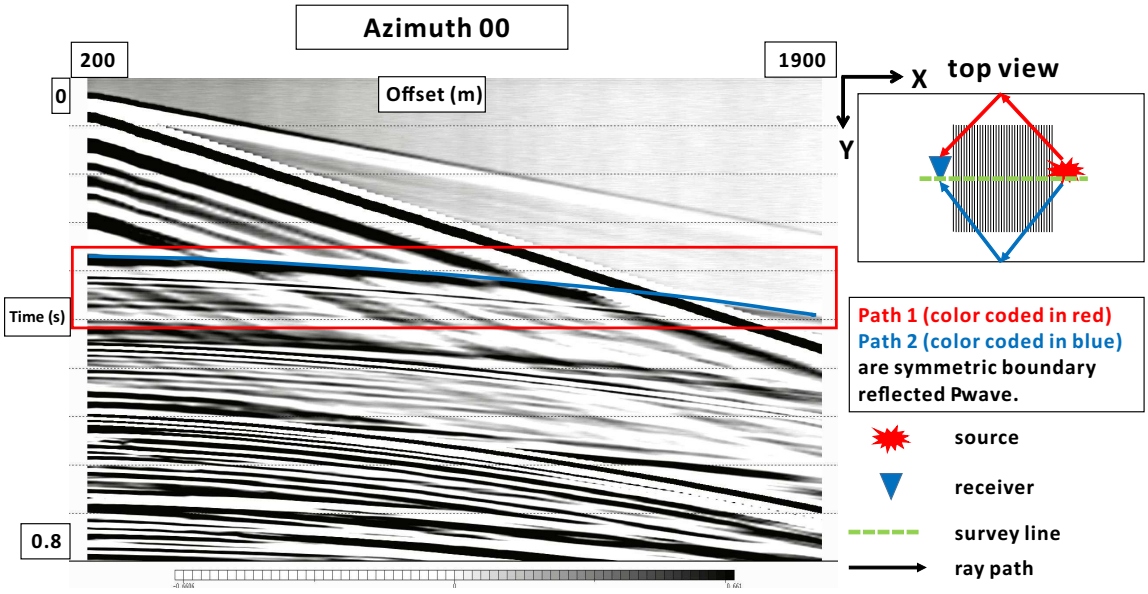

Figure 2.32: An example of boundary reflected P-wave. The red box and blue events highlighted in the data show the boundary reflected P-wave while on the right is the schematic of the ray path for this events.

1:10000 scaling which sounds absurd. Such giant source/receiver is actually averaging signals. Also, if the reflector depth is shallow, then the zero-offset we assume is not zero at all. For example, the zero offset which is define by the smallest transducer spacing we can have, is around 200 m. The reflectors of the fracture zone is 600 and 1000 m in depth. In this case, the zero offset incidence angle is 10° and 6° respectively. So we will not have reflections within this limit. On the other hand, the directivity of the transducer also puts a limit to the far offset. As showed in Figure 2.21, the transducer can record up to 35° of incidence angle. Reflections come beyond that limit might just be buried in background noise. So the problems with the transducers put an limit to the incidence angle (or offset) for recording signals. The lower limit can be improved by putting the reflector deeper while the upper limit need improvement of the transducer mechanism.

4. Multi-component. One of the advantages of physical modeling is that it can record multi-component data. However, this might also be a disadvantage since a single component transducer is not only recording single component signal at all. A vertical component transducer generates as well as records significant amount of horizontal component signals. It's the same situation for horizontal component transducer. Because of the mixture of multi-component signals from a pair of single component transducers, data processing might be tricky and sometimes problematic.

Though we have some problems with the glass model, the idea for such physical models with laser-etched fractures is enlightening and we do get some good results.

Chapter 3

3D printed models

3.1 Elastic property measurement

The 3D printed model in Allied Geophysical Laboratories were first introduced in 2011 (Figure 3.1). These models are printed with fracture layers inside. However, due to their complexity, they are not studied in this work. Here we use two small and simple models which have same size and shape but printed along different directions. Due to the layering which is created by the 3D printing mechanism, the models look like to have TI (Transversely Isotropic) symmetry. We call them "HTI model" and the "VTI model" as they stand (Figure 3.2). Both HTI and VTI models have 8 symmetric faces from the sides which allows us to measure the velocity for 45°. By measuring the length in different directions and average them, we calculate the volume of the models in assumption that the model is perfectly symmetric. Also the mass of the sample is weighted by digital scale and we measure 3 times and average

the mass. The results give the mass and volume of the HTI model as: m=104.068 g, V=108.228 $\boldsymbol{cm^3}$. Thus the density $\boldsymbol{\rho}$ is 0.962 $\boldsymbol{g/cm^3}$ using the simple relationship as $\boldsymbol{\rho = m/V}$.

Figure 3.1: Four examples of 3D printed models in AGL.

To qualitatively understand the symmetry of the models, we make an rotation experiments on the polar of the models to see how velocity change through different azimuth. Two experiments are performed on both models (HTI and VTI model) as shown in Figure 3.3, we put model in the center of the instrument and attach the transducers to the model. We rotate the transducer for every 10 degree and record the signal. Then we put the recorded signal together to generate a seismogram (Figure 3.4). From the seismogram of the HTI model, we can see clear shear-wave splitting with different azimuth which is what we expect from HTI symmetry. For VTI model, slight shear-wave splitting is observed showing that the expected isotropic plane for the TI medium is actually anisotropic indicating that the model is slightly orthorhombic. As to quantitatively understand the symmetry of the printed material (whether they can be regarded as TI or orthorhombic medium), precise measurements

of the velocities are needed.

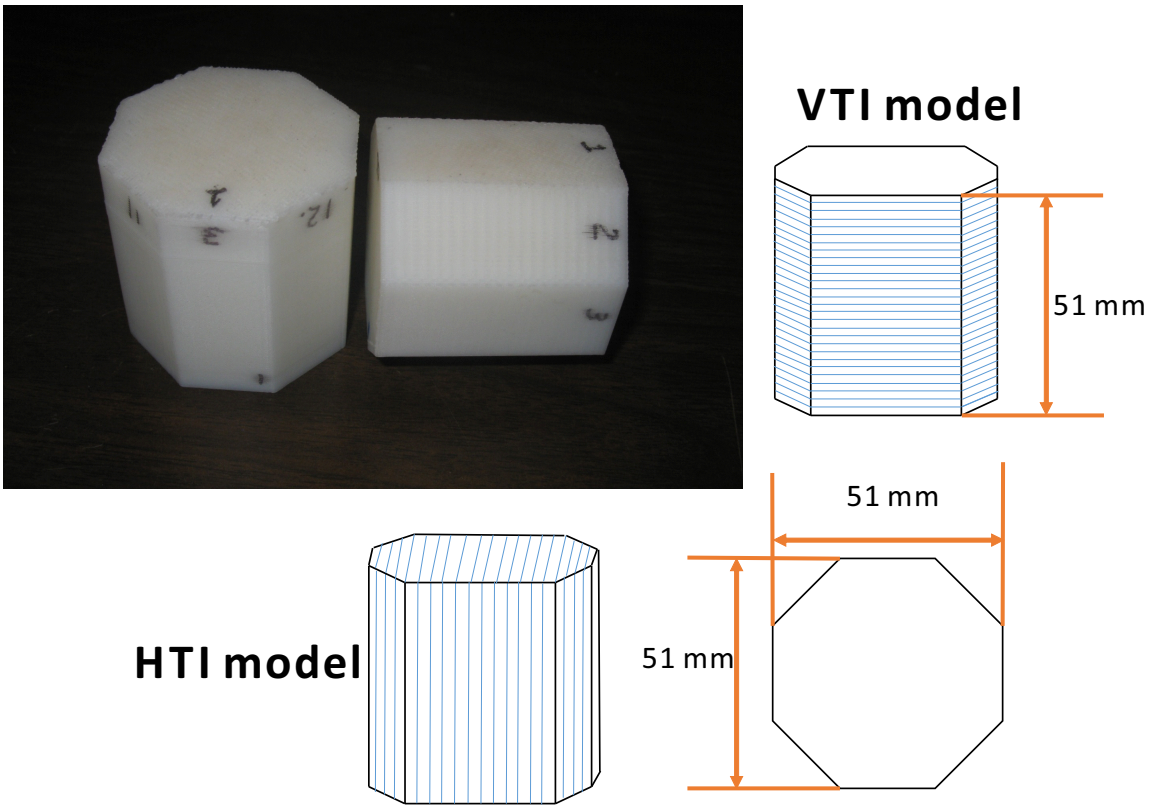

Figure 3.2: HTI and VTI models for material properties study. These two models are printed with same material and size but different bedding directions.

	HTI			VTI		
Azimuth	0°	45°	90°	0°	45°	90°
$V_P(m/s)$	1733	1745	1821	1804	1818	1828
$V_{S\parallel}(m/s)$	823	849	884	833	876	831
$V_{S\perp}(m/s)$	823	842	823	807	814	812

Table 3.1: Velocity for different azimuth.

The velocity measurement for the 3D printed models are preformed in the same way as the glass models and we do not repeat here. The results are show in Table 3.1 with different azimuth and 0° azimuth is defined as the direction along symmetry axis of the HTI model while for the VTI model, the 0° azimuth is defined as the direction where smallest P-wave velocity is observed.

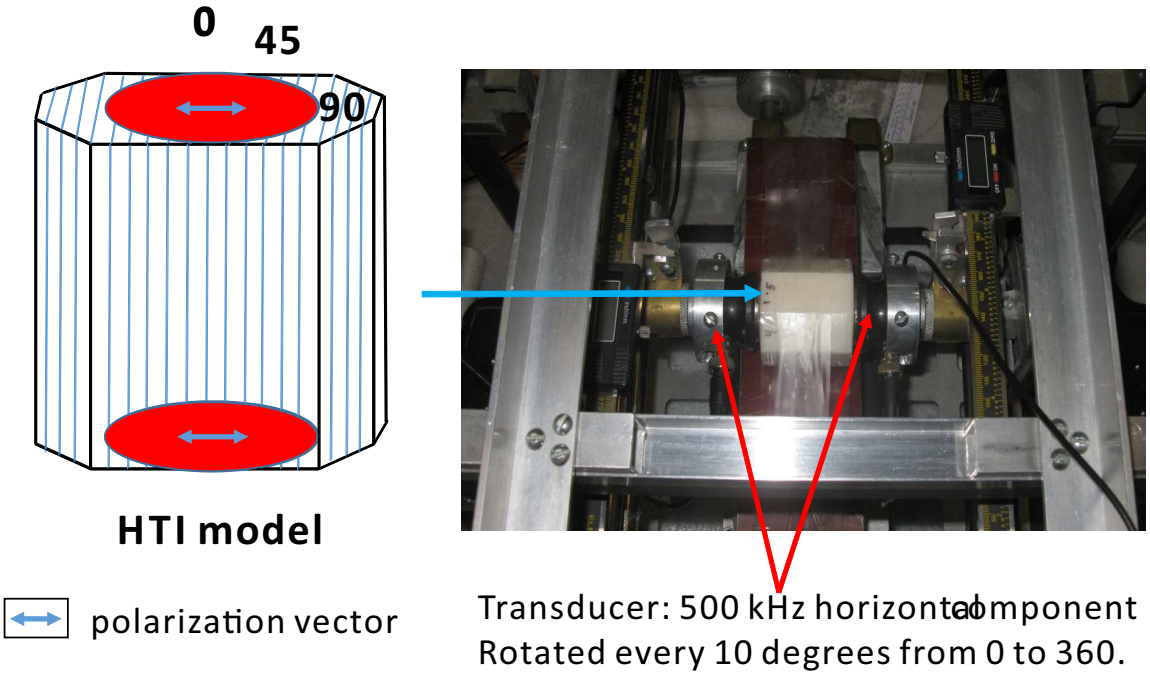

Figure 3.3: An example of rotation experiment with the HTI model. The model is attached between two transducers and the transducers are rotated every 10° from 0° to 360° and signal is recorded at each rotation angle.

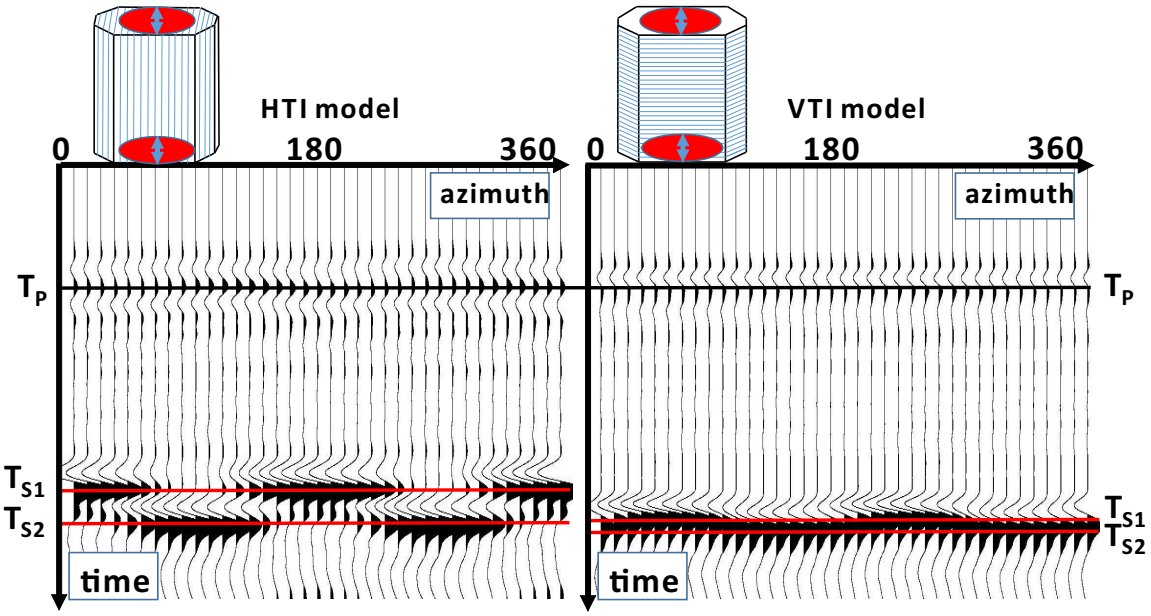

Figure 3.4: Seismogram recorded from rotation experiments of HTI and VTI model. Note that for HTI model, we can see clear shear-wave splitting with different azimuth which is what we expect from HTI symmetry. For VTI model, slightly shear-wave splitting is observed showing that the expected isotropic plane for the TI medium is actually anisotropic indicating that the model is slightly orthorhombic.

Comparing the HTI and VTI models, we find that the HTI model follows our assumption while the VTI model shows slightly orthorhombic symmetry. To study why this happens, we use microscope to see its microstructure. Figure 3.5 shows the microstructure of the 3D printed material. It's printed layer by layer but each layer symmetry goes perpendicular to each other. This geometry creates all-connected pore space as we can seen from the microstructure. In this case, what we see from the VTI azimuthal velocity is reasonable. The P-waves traveling along the two perpendicular

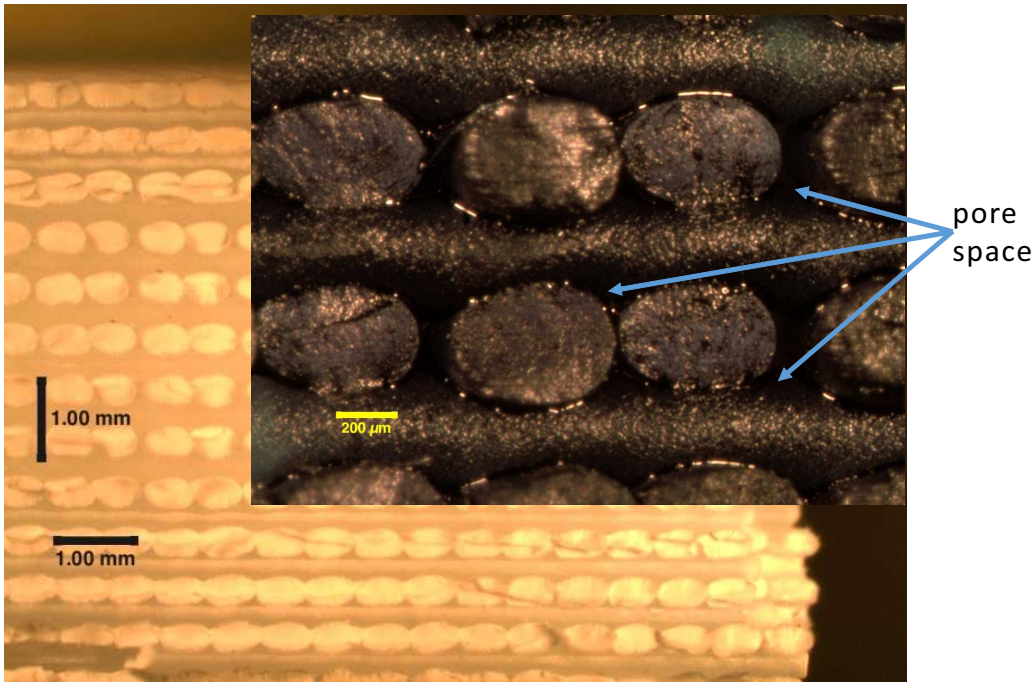

Figure 3.5: Microstructure of the 3D printed material. It's printed layer by layer but each layer symmetry goes perpendicular to each other. This geometry creates connected pore space.

directions of the fabrication symmetry in the assumed isotropic plane should have the same velocity but faster velocity in the 45° between the two directions of the fabrication symmetry. The fast shear wave polarized in the isotropic plane is also influenced by the fabrication symmetry in the same way as we see from the P-wave. However, the slow shear wave polarized perpendicular to the isotropic plane remains almost constant compared to the fast shear wave because the fabrication symmetry has very subtle influence. Besides azimuthal velocities, vertical velocities are also measured and they coincide with the azimuthal velocities due to the symmetry (Table 3.2). We see that the vertical P-wave velocity of the HTI model falls in the range of the P-wave velocity in the isotropic plane of the VTI model while the vertical P-wave

velocity of the VTI model is approximately the same with the P-wave velocity of the HTI model which is normal to isotropic planes. For the shear-wave velocities, we can find the same repeated velocities from vertical and horizontal azimuthal velocities.

Vertical velocity (m/s)	$\boldsymbol{V_P}$	$\boldsymbol{V_{S\parallel}}$	$\boldsymbol{V_{S\perp}}$
HTI	1821	884	823
VTI	1738	816	805

Table 3.2: Vertical velocity of the HTI and VTI models.

The vertical-horizontal velocity variation is about 5% while the velocity variation in the vertical isotropic plane is about 0.8%, which making it 6 times difference. In this case, we claim this material as major HTI symmetry, slightly orthorhombic.

3.2 Fluid substitution with printed HTI model

To study the fluid influence on velocity of an HTI medium, a fluid substitution experiment with the HTI model is designed. The model used in this experiment is the 3D printed HTI model. Its dry properties are measured before saturation.

3.2.1 Experiment description

The 3D printed models are anisotropic and porous making it similar to rocks. The HTI model and the VTI model show basically the same elastic property and for simplicity, we only study the HTI model for fluid substitution. Figure 3.6 shows the

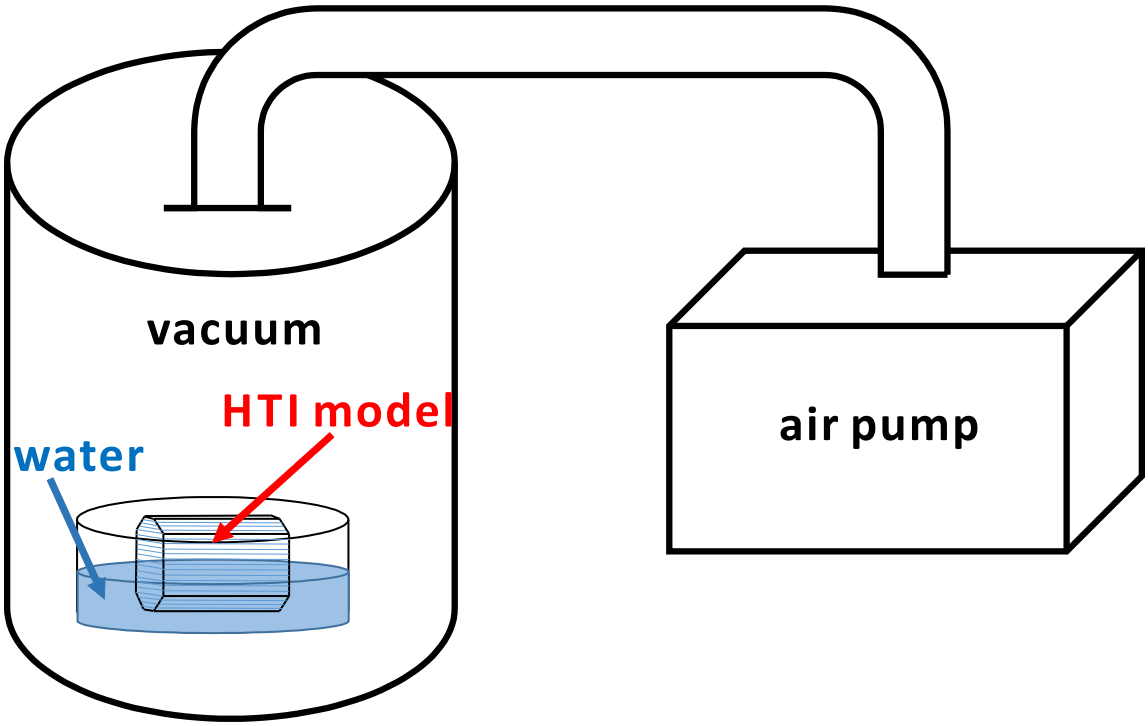

Figure 3.6: Fluid substitution experiment set-up. The HTI model is put in the tank and an air pump keeps pumping air out of the tank to make it vacuum. The air in the model is pumped out and water is sucked into the model because of capillary forces.

experiment setup, we put the HTI model in water in a bowl. Then we put the bowl in a sealed tank, we use an air pump to pump out the air out of the tank. Since there is air both in water and in HTI model, the air pump keeping pumping for about one hour until most air is pumped out. Because of the capillary force, the water is sucked into the pore space of the HTI model. After finishing the saturation experiment, we use tapes to wrap the HTI model to keep water from coming out and weight its mass after saturation to know how much water there is in the model.

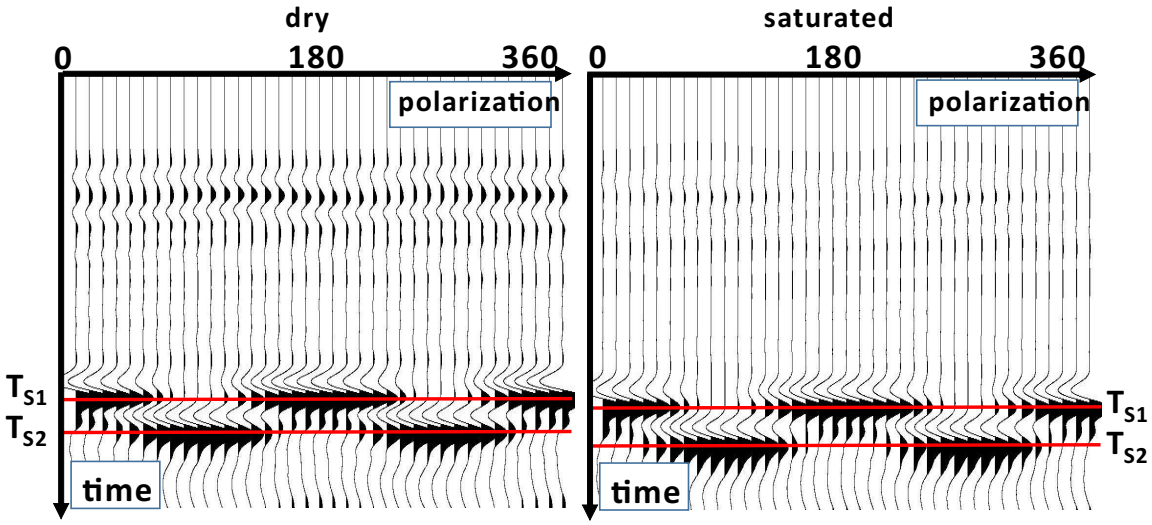

Figure 3.7: Seismogram recorded from rotation experiments of HTI model before and after fluid substitution experiment. An increase in shear wave travel time is observed indicating a velocity decrease.

3.2.2 Data

The model weights 104.068 g before saturation and 107.457 g after saturation. By subtracting the two numbers, we get the volume of water saturated in the model as 3.389 $\boldsymbol{cm^3}$. Using the definition of porosity as volume of pore space divide total volume, we calculate the porosity of the HTI model as 3.13%. Then we repeat the same experiments with the dry model. Figure 3.7 shows the seismogram recorded from rotation experiments of HTI model before and after fluid substitution experiment. We see there is change for shear-wave splitting as the traveltime is different now. Velocity in different directions are also measured. To help compare the difference, velocities measured before and after saturation are shown in Table 3.3 and Table 3.4.

	dry			water-saturated		
Azimuth	0°	45°	90°	0°	45°	90°
$\boldsymbol{V_P(m/s)}$	1733	1745	1806	1813	1818	1841
$\boldsymbol{V_{S\parallel}(m/s)}$	823	849	884	810	844	875
$\boldsymbol{V_{S\perp}(m/s)}$	823	842	823	810	838	810

Table 3.3: Velocity for different azimuth for the HTI model before and after saturation.

Vertical velocity (m/s)	$\boldsymbol{V_P}$	$\boldsymbol{V_{S\parallel}}$	$\boldsymbol{V_{S\perp}}$
dry	1821	884	823
water-saturated	1856	874	810

Table 3.4: Vertical velocity of the HTI models before and after saturation.

3.3 Theory and method

The general equations for fluid dependency of the elastic moduli of anisotropic media were first given by Gassmann (1951). For the case of an HTI medium, Gurevich (2003) derived the explicit equations based on a linear-slip model. Gurevich's complex equations are recast here in a more accessible format. Those equations depend on four parameters: $\boldsymbol{\lambda}$, $\boldsymbol{\mu}$, $\boldsymbol{\Delta_N}$ and $\boldsymbol{\Delta_T}$. They are quite similar to the well-known isotropic Gassmann's equations. We also propose a valid method for the application of these equations.

3.3.1 Introduction

Fluid substitution in rocks is very important for understanding their fluid-dependent seismic response. The most commonly used method for fluid substation comes from the work of Gassmann (1951), which relates the bulk modulus of a rock to its porosity, rock matrix and fluid properties. His equations (Smith et al., 2003) can be written as:

$$\boldsymbol{K^{sat} = K + \frac{(1 - K/K_m)^2}{\phi/K_{fl} + (1-\phi)/K_m - K/K_m^2}}, \tag{3.1}$$

where $\boldsymbol{\phi}$ is the porosity, $\boldsymbol{K^{sat}}$ = the saturated bulk modulus, $\boldsymbol{K_m}$ = the bulk modulus of the mineral matrix, $\boldsymbol{K_{fl}}$ = the bulk modulus of the pore fluid, $\boldsymbol{K}$ = the bulk modulus of the drained porous rock frame. Most of the applications of fluid substitution are based on the assumption of an isotropic rock model, which may not be quite the real case. We know that many reservoirs are fractured, and therefore anisotropic to some extent. Actually, Gassmann (1951) also published a general equation for anisotropic fluid substitution. His results can be written in terms of stiffness tensors, $\boldsymbol{C_{ijkl}}$, where a repeated index implies a sum over 1-3 (Mavko and Bandyopadhyay, 2009):

$$\boldsymbol{C^{sat}_{ijkl} = C_{ijkl} + \frac{(K_m\delta_{ij} - C_{ij\alpha\alpha}/3)(K_m\delta_{ij} - C_{\beta\beta kl}/3)}{(K_m/K_{fl})\phi(K_m - K_{fl}) + (K_m - C_{ppqq}/9)}}, \tag{3.2}$$

where,

$$\boldsymbol{\delta_{ij}} = \begin{cases} \mathbf{1}, & \text{i = j} \\ \mathbf{0}, & \text{i} \neq \text{j} \end{cases}, \tag{3.3}$$

$$\boldsymbol{C_{ppqq} = \sum_{p=1}^{3}\sum_{q=1}^{3} C_{ppqq}}, \tag{3.4}$$

$$\boldsymbol{C_{ij\alpha\alpha}} = \sum_{\boldsymbol{i=1}}^{\boldsymbol{3}} \sum_{\boldsymbol{j=1}}^{\boldsymbol{3}} \sum_{\boldsymbol{\alpha=1}}^{\boldsymbol{3}} \boldsymbol{C_{ij\alpha\alpha}}, \tag{3.5}$$

From Equation 3.2, we can see that to perform Gassmann's anisotropic fluid substitution equations, we need to know all the stiffness tensors of the rock and we seldom have enough measurements. In this case, these equations become useless and people have to choose isotropic equations for the anisotropic rocks as an approximation. In order to use the anisotropic formulation, some rock models are proposed and people derived different approximations for Gassmann's equations. Gurevich (2003) and Sil et al. (2011) derived the anisotropic Gassmann's equations for an HTI rock based on a linear-slip model (Hsu and Schoenberg, 1993; Schoenberger and Sayers, 1995) and analyzed the effect of changing porosity and water saturation. However, the equations they gave are difficult to understand intuitively. Mavko and Bandyopadhyay (2009) derived an approximate fluid substitution for vertical velocities in weakly anisotropic VTI rocks. They used the vertical velocity to calculate the bulk modulus of "the anisotropic material having the same velocities as the observed vertical VTI velocities". This calculation seems to assume that the vertical velocity of the VTI rocks is the velocity of the isotropic background rocks. Their approximations for the anisotropic Gassmann's equations are very similar to the isotropic case, but with a first-order correction proportional to Thomsen's parameter $\boldsymbol{\delta}$ (Thomsen, 1986). They used the variation of $\boldsymbol{\delta}$ to explain why isotropic fluid substitution underpredicts or overpredicts the anisotropic results. In our study, we derive approximations for the anisotropic Gassmann's equations for HTI rocks based on the linear-slip model. We use the vertical velocities as an approximation to calculate the bulk modulus of the isotropic background (Sil, 2013).

The results are quite similar to the form of the isotropic case. Also, we propose a practical method for implementing these equations and use synthetic data as an example to test our equations.

3.3.2 HTI medium

In an HTI medium, vertical fractures are embedded along a preferred orientation (normal to fracture planes) in an isotropic background (Figure 3.8). The fractured rocks (or the HTI medium) can be considered as a simple combination of fractures and isotropic rocks (Hsu and Schoenberg, 1993).

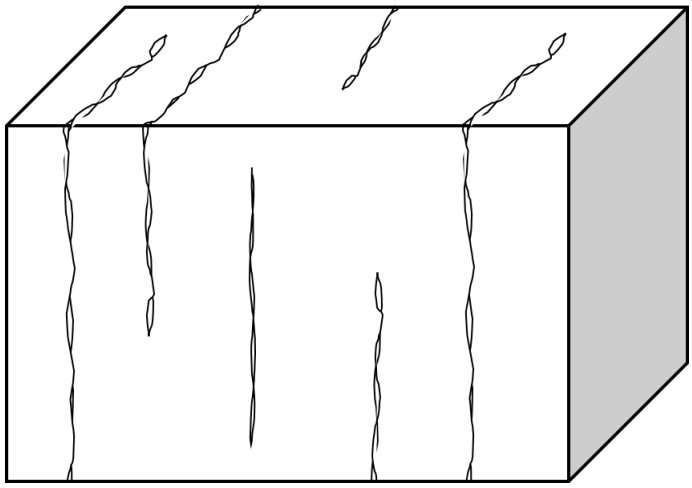

Figure 3.8: A cartoon representation of an HTI medium which consists of an isotropic background rock and a set of oriented fractures. The symmetry axis of the medium is normal to the fracture planes.

The isotropic rocks are characterized by Lamé parameter ($\boldsymbol{\lambda}$) and shear modulus ($\boldsymbol{\mu}$) while the imbedded fractures are characterized with the dimensionless normal

and tangential fracture weakness, $\boldsymbol{\Delta_N}$ and $\boldsymbol{\Delta_T}$, respectively. By using these four parameters, we can characterize the HTI medium instead of the five independent stiffness tensors under the constraint that (Schoenberger and Sayers, 1995):

$$\boldsymbol{C_{11}C_{33} - C_{13}^2 = 2C_{44}(C_{11} + C_{13}),} \tag{3.6}$$

For such an anisotropic rock model, expressions for the dry stiffness matrix can be written as (Schoenberger and Sayers, 1995):

$$\boldsymbol{C_{ij}} = \begin{pmatrix} \boldsymbol{C_{11}} & \boldsymbol{C_{13}} & \boldsymbol{C_{13}} & \mathbf{0} & \mathbf{0} & \mathbf{0} \\ \boldsymbol{C_{13}} & \boldsymbol{C_{33}} & \boldsymbol{C_{23}} & \mathbf{0} & \mathbf{0} & \mathbf{0} \\ \boldsymbol{C_{13}} & \boldsymbol{C_{23}} & \boldsymbol{C_{33}} & \mathbf{0} & \mathbf{0} & \mathbf{0} \\ \mathbf{0} & \mathbf{0} & \mathbf{0} & \boldsymbol{C_{44}} & \mathbf{0} & \mathbf{0} \\ \mathbf{0} & \mathbf{0} & \mathbf{0} & \mathbf{0} & \boldsymbol{C_{55}} & \mathbf{0} \\ \mathbf{0} & \mathbf{0} & \mathbf{0} & \mathbf{0} & \mathbf{0} & \boldsymbol{C_{55}} \end{pmatrix} = \left(\begin{array}{c|c} \mathbf{C_1} & \mathbf{0} \\ \hline \mathbf{0} & \mathbf{C_2} \end{array}\right), \tag{3.7}$$

where $\mathbf{0}$ is the $3\times$ 3 zero matrix and $\mathbf{C_1}$ and $\mathbf{C_2}$ are given by

$$\mathbf{C_1} = \begin{pmatrix} \boldsymbol{M(1-\Delta_N)} & \boldsymbol{\lambda(1-\Delta_N)} & \boldsymbol{\lambda(1-\Delta_N)} \\ \boldsymbol{\lambda(1-\Delta_N)} & \boldsymbol{M(1-r^2\Delta_N)} & \boldsymbol{\lambda(1-r\Delta_N)} \\ \boldsymbol{\lambda(1-\Delta_N)} & \boldsymbol{\lambda(1-r\Delta_N)} & \boldsymbol{M(1-r^2\Delta_N)} \end{pmatrix}, \tag{3.8}$$

and

$$\mathbf{C_2} = \begin{pmatrix} \boldsymbol{\mu} & \mathbf{0} & \mathbf{0} \\ \mathbf{0} & \boldsymbol{\mu(1-\Delta_T)} & \mathbf{0} \\ \mathbf{0} & \mathbf{0} & \boldsymbol{\mu(1-\Delta_T)} \end{pmatrix}, \tag{3.9}$$

where,

$$\boldsymbol{M = \lambda + 2\mu,} \tag{3.10}$$

$$r = \lambda/(\lambda + 2\mu), \tag{3.11}$$

$$\Delta_N = Z_N M/(1 + Z_N M), \tag{3.12}$$

$$\Delta_T = Z_T \mu/(1 + Z_T \mu), \tag{3.13}$$

In the equations above, Z_N and Z_T are the normal and tangential fracture compliances of the anisotropic fractured rocks. With the stiffness matrix of the dry rock, we can derive the expressions for $C_{1\alpha}$ and C_{pq}, and substitute them into equation 3.2, to get the explicit expressions for HTI Gassmann's equations. Here we take C_{11}^{sat} for example.

From equation 3.2, we can write C_{11}^{sat} as:

$$C_{11}^{sat} = C_{11} + \frac{(K_m - C_{1\alpha}/3)^2}{(K_m/K_{fl})\phi(K_m - K_{fl}) + (K_m - C_{pq}/9)}, \tag{3.14}$$

Using equation 3.8, 3.10 and 3.11, we can express the following quantities as

$$C_{1\alpha} = 3K(1 - \Delta_N), \tag{3.15}$$

$$C_{pq} = 9K(1 - \Delta_N K/M), \tag{3.16}$$

where $K = \lambda + 2/3\mu$ is the bulk modulus of the background isotropic rock .

Substituting equations 3.15 and 3.16 into equation 3.14, we have:

$$\begin{aligned} C_{11}^{sat} &= M(1 - \Delta_N) \\ &\quad + \frac{(K_m - K(1 - \Delta_N))^2}{(K_m/K_{fl})\phi(K_m - K_{fl}) + K_m - K + \Delta_N K^2/M} \end{aligned} \tag{3.17}$$

The results are very similar to the isotropic Gassmann's equation: the first part is the stiffness tensor of the dry rock and the second part is almost same as the isotropic Gassmann's equation except that we have one more term for the fractures. We can derive other stiffness tensors of the saturated rocks in a similar way, given:

$$\boldsymbol{C_{2\alpha} = C_{3\alpha} = 3K(1 - r\Delta_N),} \tag{3.18}$$

$$\boldsymbol{C_{4\alpha} = C_{5\alpha} = C_{6\alpha} = 0,} \tag{3.19}$$

The results are:

$$\begin{aligned} \boldsymbol{C_{33}^{sat}} &= \boldsymbol{M(1 - r^2\Delta_N)} \\ &+ \frac{\boldsymbol{(K_m - K(1 - r\Delta_N))^2}}{\boldsymbol{(K_m/K_{fl})\phi(K_m - K_{fl}) + (K_m - K + \Delta_N K^2/M)}} \end{aligned} \tag{3.20}$$

$$\begin{aligned} \boldsymbol{C_{13}^{sat}} &= \boldsymbol{\lambda(1 - \delta_N)} \\ &+ \frac{\boldsymbol{(K_m - K(1 - \Delta_N))(K_m - K(1 - r\Delta_N))}}{\boldsymbol{(K_m/K_{fl})\phi(K_m - K_{fl}) + (K_m - K + \Delta_N K^2/M)}} \end{aligned} \tag{3.21}$$

$$\boldsymbol{C_{44}^{sat} = \mu,} \tag{3.22}$$

$$\boldsymbol{C_{55}^{sat} = \mu(1 - \Delta_T),} \tag{3.23}$$

By using equation 3.17 and 3.20-3.23, we can perform anisotropic fluid substitution analysis.

3.3.3 Orthorhombic medium

Almost same derivation could be performed with orthorhombic case. Here we consider the orthorhombic symmetry which comes from an isotropic background

with two vertically aligned sets of fractures orthogonal to each other. For such a medium, Bakulin et al. (2000b) derived the effective stiffness matrix using linear slip theory (Equation 3.24).

$$\boldsymbol{C_{ij}} = \begin{pmatrix} \boldsymbol{C_{11}} & \boldsymbol{C_{12}} & \boldsymbol{C_{13}} & \mathbf{0} & \mathbf{0} & \mathbf{0} \\ \boldsymbol{C_{12}} & \boldsymbol{C_{22}} & \boldsymbol{C_{23}} & \mathbf{0} & \mathbf{0} & \mathbf{0} \\ \boldsymbol{C_{13}} & \boldsymbol{C_{23}} & \boldsymbol{C_{33}} & \mathbf{0} & \mathbf{0} & \mathbf{0} \\ \mathbf{0} & \mathbf{0} & \mathbf{0} & \boldsymbol{C_{44}} & \mathbf{0} & \mathbf{0} \\ \mathbf{0} & \mathbf{0} & \mathbf{0} & \mathbf{0} & \boldsymbol{C_{55}} & \mathbf{0} \\ \mathbf{0} & \mathbf{0} & \mathbf{0} & \mathbf{0} & \mathbf{0} & \boldsymbol{C_{66}} \end{pmatrix} = \left(\begin{array}{c|c} \mathbf{C_1} & \mathbf{0} \\ \hline \mathbf{0} & \mathbf{C_2} \end{array} \right), \tag{3.24}$$

where $\mathbf{0}$ is the $3\times$ 3 zero matrix and $\mathbf{C_1}$ and $\mathbf{C_2}$ are given by

$$\mathbf{C_1} = \frac{\mathbf{1}}{\boldsymbol{d}} \begin{pmatrix} \boldsymbol{M l_1 m_3} & \boldsymbol{\lambda l_1 m_1} & \boldsymbol{\lambda l_1 m_2} \\ \boldsymbol{\lambda l_1 m_1} & \boldsymbol{M l_3 m_1} & \boldsymbol{\lambda l_2 m_1} \\ \boldsymbol{\lambda l_1 m_2} & \boldsymbol{\lambda l_2 m_1} & \boldsymbol{M(l_3 m_3 - l_4)} \end{pmatrix}, \tag{3.25}$$

and

$$\mathbf{C_2} = \begin{pmatrix} \boldsymbol{\mu(1-\Delta_{T2})} & \mathbf{0} & \mathbf{0} \\ \mathbf{0} & \boldsymbol{\mu(1-\Delta_{T1})} & \mathbf{0} \\ \mathbf{0} & \mathbf{0} & \boldsymbol{\mu \frac{(1-\Delta_{T1})(1-\Delta_{T2})}{(1-\Delta_{T1}\Delta_{T2})}} \end{pmatrix}, \tag{3.26}$$

where,

$$\boldsymbol{l_1 = 1 - \Delta_{N1}}, \tag{3.27}$$

$$\boldsymbol{l_2 = 1 - r\Delta_{N1}}, \tag{3.28}$$

$$\boldsymbol{l_3 = 1 - r^2\Delta_{N1}}, \tag{3.29}$$

$$l_4 = 4r^2g^2\Delta_{N1}\Delta_N 2, \tag{3.30}$$

$$m_1 = 1 - r^2\Delta_{N2}, \tag{3.31}$$

$$m_2 = 1 - r\Delta_{N2}, \tag{3.32}$$

$$m_3 = 1 - r^2\Delta_{N2}, \tag{3.33}$$

$$g = \mu/(\lambda + 2\mu) = V_s^2/V_p^2, \tag{3.34}$$

$$d = 1 - r^2\Delta_{N1}\Delta_{N2}, \tag{3.35}$$

$$\Delta_{Ni} = Z_{Ni}M/(1 + Z_{Ni}M), \tag{3.36}$$

$$\Delta_{Ti} = Z_{Ti}\mu/(1 + Z_{Ti}\mu), \tag{3.37}$$

In the equations above, Δ_{Ni} and Δ_{Ti} (i=1,2) are the normal and tangential fracture weakness (defined in the same way as the HTI case) of the anisotropic fractured rocks. For such equivalence to be valid, three additional relationships should be satisfied:

$$C_{12}C_{33} + C_{23} = C_{13}(C_{22} + C_{23}), \tag{3.38}$$

$$2(C_{11} + C_{13}) = (C_{11}C_{33} - C_{13}^2)(\frac{C_{44} + C_{55}}{C_{44}C_{55}} - \frac{1}{C_{66}}), \tag{3.39}$$

and

$$2(C_{22} + C_{23}) = (C_{22}C_{33} - C_{23}^2)(\frac{C_{44} + C_{55}}{C_{44}C_{55}} - \frac{1}{C_{66}}), \tag{3.40}$$

With the effective stiffness matrix of the dry rock, we can derive the expressions for $\boldsymbol{C_{1\alpha}}$ and $\boldsymbol{C_{pq}}$, and substitute them into equation 3.2, to get the explicit expressions for orthorhombic Gassmann's equations. Using equations above, we can express the following quantities (second-order terms are dropped) as

$$\boldsymbol{C_{1\alpha} = 3K(1 - \Delta_{N1} - r\Delta_{N2}),} \tag{3.41}$$

$$\boldsymbol{C_{2\alpha} = 3K(1 - r\Delta_{N1} - \Delta_{N2}),} \tag{3.42}$$

$$\boldsymbol{C_{3\alpha} = 3K(1 - r\Delta_{N1} - r\Delta_{N2}),} \tag{3.43}$$

$$\boldsymbol{C_{4\alpha} = C_{5\alpha} = C_{6\alpha} = 0,} \tag{3.44}$$

$$\boldsymbol{C_{pq} = 9K(1 - \frac{K(\Delta_{N1} + \Delta_{N2})}{\lambda + 2\mu}),} \tag{3.45}$$

By Substituting above equations into each $\boldsymbol{C_{ij}^{sat}}$, we have:

$$\begin{aligned} \boldsymbol{C_{11}^{sat}} &= \boldsymbol{M(1 - \Delta_{N1} - r^2\Delta_{N2})} \\ &\quad + \frac{\boldsymbol{(K_m - K(1 - \Delta_{N1} - r\Delta_{N2}))^2}}{\boldsymbol{(K_m/K_{fl})\phi(K_m - K_{fl}) + K_m - K - K^2(\Delta_{N1} + \Delta_{N2})/M}} \end{aligned} \tag{3.46}$$

$$\begin{aligned} \boldsymbol{C_{22}^{sat}} &= \boldsymbol{M(1 - r^2\Delta_{N1} - \Delta_{N2})} \\ &\quad + \frac{\boldsymbol{(K_m - K(1 - r\Delta_{N1} - \Delta_{N2}))^2}}{\boldsymbol{(K_m/K_{fl})\phi(K_m - K_{fl}) + K_m - K - K^2(\Delta_{N1} + \Delta_{N2})/M}} \end{aligned} \tag{3.47}$$

$$C_{33}^{sat} = M(1 - r^2\Delta_{N1} - r^2\Delta_{N2}) + \frac{(K_m - K(1 - r\Delta_{N1} - r\Delta_{N2}))^2}{(K_m/K_{fl})\phi(K_m - K_{fl}) + K_m - K - K^2(\Delta_{N1} + \Delta_{N2})/M} \tag{3.48}$$

$$C_{12}^{sat} = M(1 - \Delta_{N1} - \Delta_{N2}) + \frac{(K_m - K(1 - \Delta_{N1} - r\Delta_{N2}))(K_m - K(1 - r\Delta_{N1} - \Delta_{N2}))}{(K_m/K_{fl})\phi(K_m - K_{fl}) + K_m - K - K^2(\Delta_{N1} + \Delta_{N2})/M} \tag{3.49}$$

$$C_{13}^{sat} = M(1 - \Delta_{N1} - \Delta_{N2}) + \frac{(K_m - K(1 - \Delta_{N1} - r\Delta_{N2}))(K_m - K(1 - r\Delta_{N1} - r\Delta_{N2}))}{(K_m/K_{fl})\phi(K_m - K_{fl}) + K_m - K - K^2(\Delta_{N1} + \Delta_{N2})/M} \tag{3.50}$$

$$C_{23}^{sat} = M(1 - \Delta_{N1} - \Delta_{N2}) + \frac{(K_m - K(1 - r\Delta_{N1} - \Delta_{N2}))(K_m - K(1 - r\Delta_{N1} - r\Delta_{N2}))}{(K_m/K_{fl})\phi(K_m - K_{fl}) + K_m - K - K^2(\Delta_{N1} + \Delta_{N2})/M} \tag{3.51}$$

$$C_{44}^{sat} = \mu(1 - \Delta_{T2}), \tag{3.52}$$

$$C_{55}^{sat} = \mu(1 - \Delta_{T1}), \tag{3.53}$$

$$C_{66}^{sat} = \mu\frac{(1 - \Delta_{T1})(1 - \Delta_{T2})}{(1 - \Delta_{T1}\Delta_{T2})}, \tag{3.54}$$

By using equation 3.46 to 3.54, we can perform anisotropic fluid substitution analysis for an orthorhombic medium.

3.3.4 Method

Before performing the anisotropic Gassmann's equations to an HTI medium with the new expressions, we need to know the four parameters: $\boldsymbol{\lambda}$, $\boldsymbol{\mu}$, $\boldsymbol{\delta_N}$ and $\boldsymbol{\delta_T}$. There are some assumptions: 1) The vertical P- and fast S-wave velocities of the HTI medium are the same to the isotropic background (Sil, 2013); 2) All the pores that contribute the porosity in our equations are interconnected; 3) The fluid diffusion length is larger than the fracture size and spacing (Gurevich, 2003) which means the low frequency limit; 4) The HTI medium agrees with the linear-slip model assumption. Bakulin et al. (2000a) gave a comparison between linear-slip model and Hudson's penny-shaped model for the case of an HTI medium. They concluded that by satisfying some relations, these two models could become identical and lead to the same results. Figure 3.9 shows the work flow for parameter estimation. The vertical velocities of the P-wave, the fast and slow S-wave, and density of the background isotropic rocks can be obtained from a vertical well-log data. With these parameters, we can invert for Lamé parameter, $\boldsymbol{\lambda}$, and shear modulus, $\boldsymbol{\mu}$, as well as $\boldsymbol{C_{33}}$, $\boldsymbol{C_{44}}$ and $\boldsymbol{C_{55}}$ of the dry anisotropic rocks based on the method developed by Sil (2013). As for the calculation of the tangential fracture compliance, $\boldsymbol{Z_T}$, the expression was given by Hsu and Schoenberg (1993) for a VTI medium as:

$$\boldsymbol{Z_T^{VTI}} = \frac{\mathbf{1}}{\boldsymbol{C_{44}^{VTI}}} - \frac{\mathbf{1}}{\boldsymbol{C_{66}^{VTI}}}, \tag{3.55}$$

We know that VTI and HTI medium are equivalent in case of a 90° rotated symmetry axis. So we can use this result and transform it from VTI to HTI medium:

$$\boldsymbol{Z_T} = \frac{\mathbf{1}}{\boldsymbol{C_{55}}} - \frac{\mathbf{1}}{\boldsymbol{C_{44}}}, \tag{3.56}$$

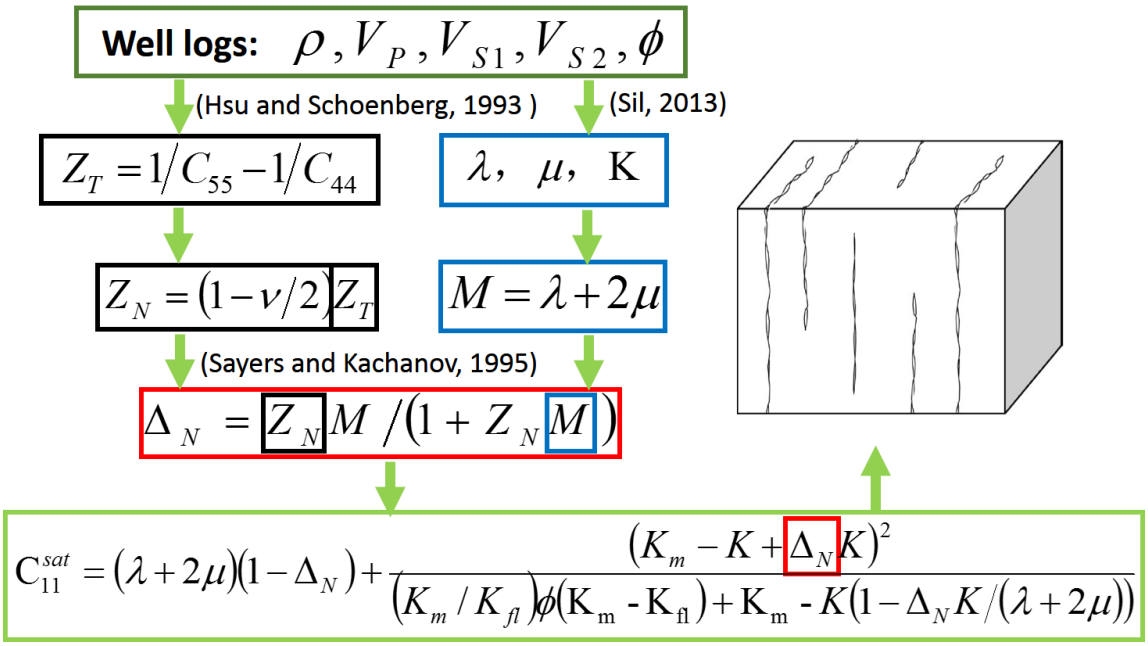

Figure 3.9: Work flow for parameter estimation using well log data. Vertical velocities are assumed to be the background matrix velocities.

With $\boldsymbol{Z_T}$, using the relation defined by Sayers and Kachanov (1995), we can write:

$$\frac{\boldsymbol{Z_N}}{\boldsymbol{Z_T}} = \mathbf{1} - \frac{\boldsymbol{\nu}}{\mathbf{2}}, \tag{3.57}$$

where $\boldsymbol{\nu}$ is the background isotropic rock's Poisson's ratio of the background isotropic rock which can be derived from the vertical P- and fast S-wave velocities. Generally, obtaining the background P-wave velocity requires analysis of the unfractured core samples. However, for practical purposes, we can consider the vertical P-wave velocity to be equal to the background isotropic P-wave velocity (Prioul et al., 2007). This assumption works well when the normal fracture weakness values are relatively small. Then by substituting the values of $\boldsymbol{\lambda}$, $\boldsymbol{\mu}$, $\boldsymbol{Z_N}$ and $\boldsymbol{Z_T}$, we can obtain the values of the normal and tangential fracture weakness $\boldsymbol{\delta_N}$ and $\boldsymbol{\delta_T}$. Now, knowing how to calculate the four parameters, we are ready to test the new equations. As the

method for the case of orthorhombic symmetry, it is much more complicated and is not studied in this thesis as how to perform the fluid substitution.

3.3.5 Synthetic data test

The synthetic data are generated with the General Singular Approximation (GSA) method, which can be used to calculate the effective stiffness (Shermergor, 1977). The GSA method is applicable for a large inclusion concentration, pore connection and arbitrary ellipsoidal shape of pores and cracks (Jiang and Chesnokov, 2012). The friability parameter in GSA method ranges from 0 to 1, meaning pores are all closed for 0 or all connected for 1. GSA shows good agreement with Rathore's synthetic sandstone measurement (Rathore et al., 1995; Bayuk and Chesnokov, 1998). Thus, we decided to use GSA method to generate the data for testing different HTI Gassmann algorithms. The synthetic sandstone model is based on Rathore's model. The friability is set to 1, which is required by the assumption of all pores being connected in Gassmann fluid substitution (Smith et al., 2003). The synthetic sandstone model is a two-phase model composed of matrix and cracks. The matrix is a mixture of sand and epoxy, with bulk modulus of 5.21 GPa, shear modulus of 4.17 GPa and density of 1.712 g/cc. The cracks are penny-shaped cracks with thickness of 0.02 mm, diameter of 1 mm and aspect ratio of 1/50. The crack density is 0.018. Thus we can calculate the porosity of cracks which is 0.15% by using $\boldsymbol{N_c} = 3\boldsymbol{\phi}/4\boldsymbol{\pi}\boldsymbol{\chi}$, here Nc is crack density, $\boldsymbol{\phi}$ is porosity of cracks and $\boldsymbol{\chi}$ is the aspect ratio of cracks. The bulk moduli and densities are 0.0001 GPa, 0.0007 g/cc for gas and 2.16 GPa, 1 g/cc for water. We start with the GSA effective stiffness of the dry model and

input them into the exact Gassmann's equations (Equations 3.2), the GSA method, our HTI Gassmann approximation as well as the one from Gurevich (2003), and then compare the output results for the four different algorithms of the saturated synthetic model. For the dry model, $\boldsymbol{C_{11}} = 1.03$ GPa; $\boldsymbol{C_{13}} = 0.30$ GPa; $\boldsymbol{C_{33}} = 10.24$ GPa; $\boldsymbol{C_{44}} = 4.15$ GPa; $\boldsymbol{C_{55}} = 0.78$ GPa. The results are shown in Figure 3.10 and we find that our algorithm matches well with the exact Gassmann's equations and the GSA method. However, we should note that Gassmann's equations assume that shear rigidity remains constant regardless of fluid type. And in our results, the slow shear wave velocity is determined by the tangential fracture weakness, $\boldsymbol{\delta_T}$, which is approximated. In this case, our approximation might introduce variations to slow shear wave velocity because of fluid substitution, which is different from the exact Gassmann's prediction. Apart from the confusions we may have from the equations, we think that the anisotropic Gassmann's equations are valid for predicting P-wave velocity, but the shear wave velocity predicted by Gassmann must not be realistic. We also study the changes in the P-wave moduli and velocities of an HTI medium as a function of porosity and water saturation (Sw) using our equations. The model parameters are the same with the above synthetic sandstone model. In Figure 3.11, we plot the $\boldsymbol{C_{11}}$ and $\boldsymbol{C_{33}}$ values with increasing porosity and the water saturation is set to 100% (top panel). We can see that the P-wave moduli decrease with increasing porosity and $\boldsymbol{C_{11}}$ is more sensitive to porosity than $\boldsymbol{C_{33}}$.

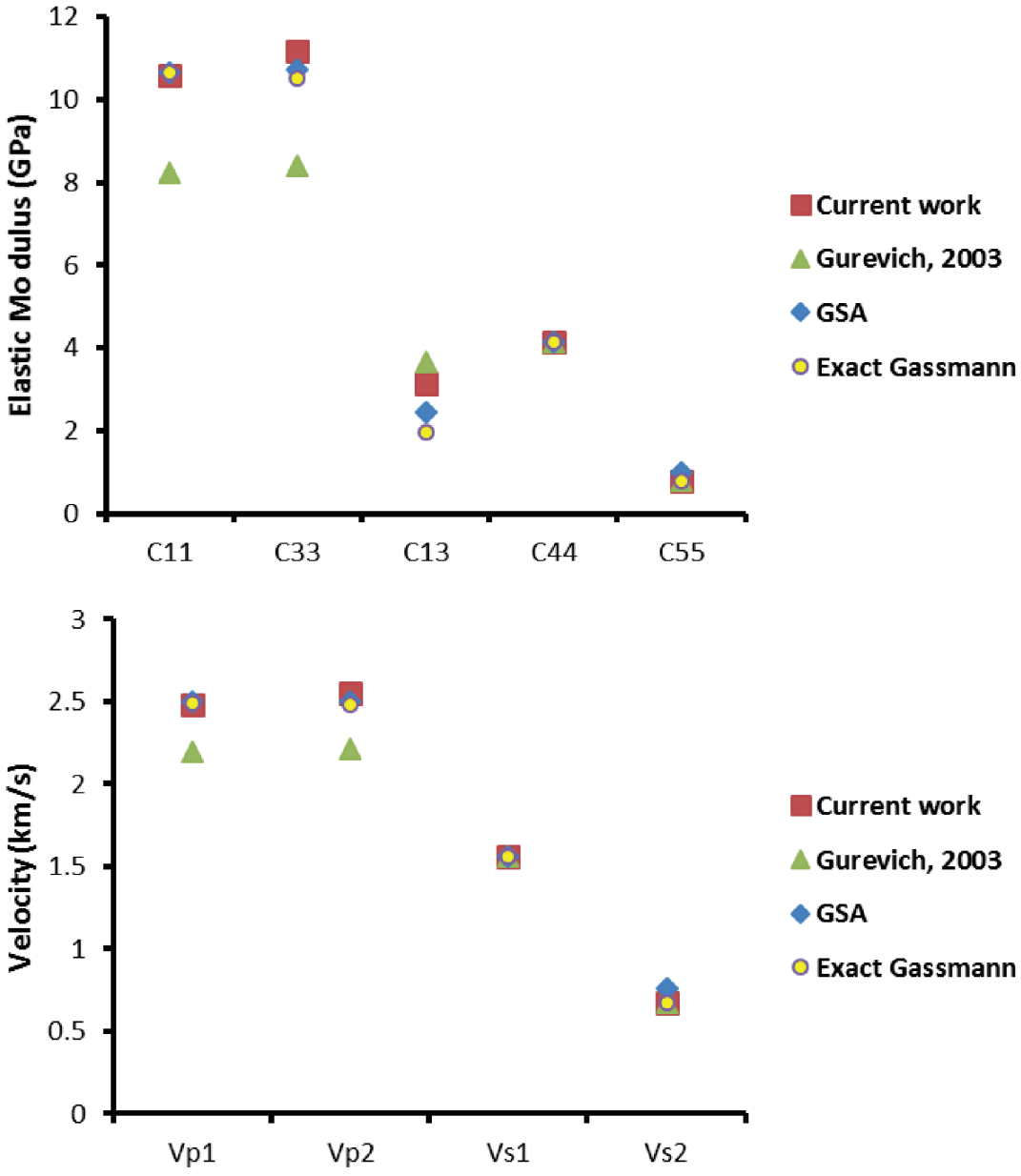

Figure 3.10: Comparisons of the results from four different algorithms for the saturated synthetic sandstone model. Top panel shows the comparison results for the five elastic moduli. Bottom panel shows the comparison results for the P- and S-wave velocities.

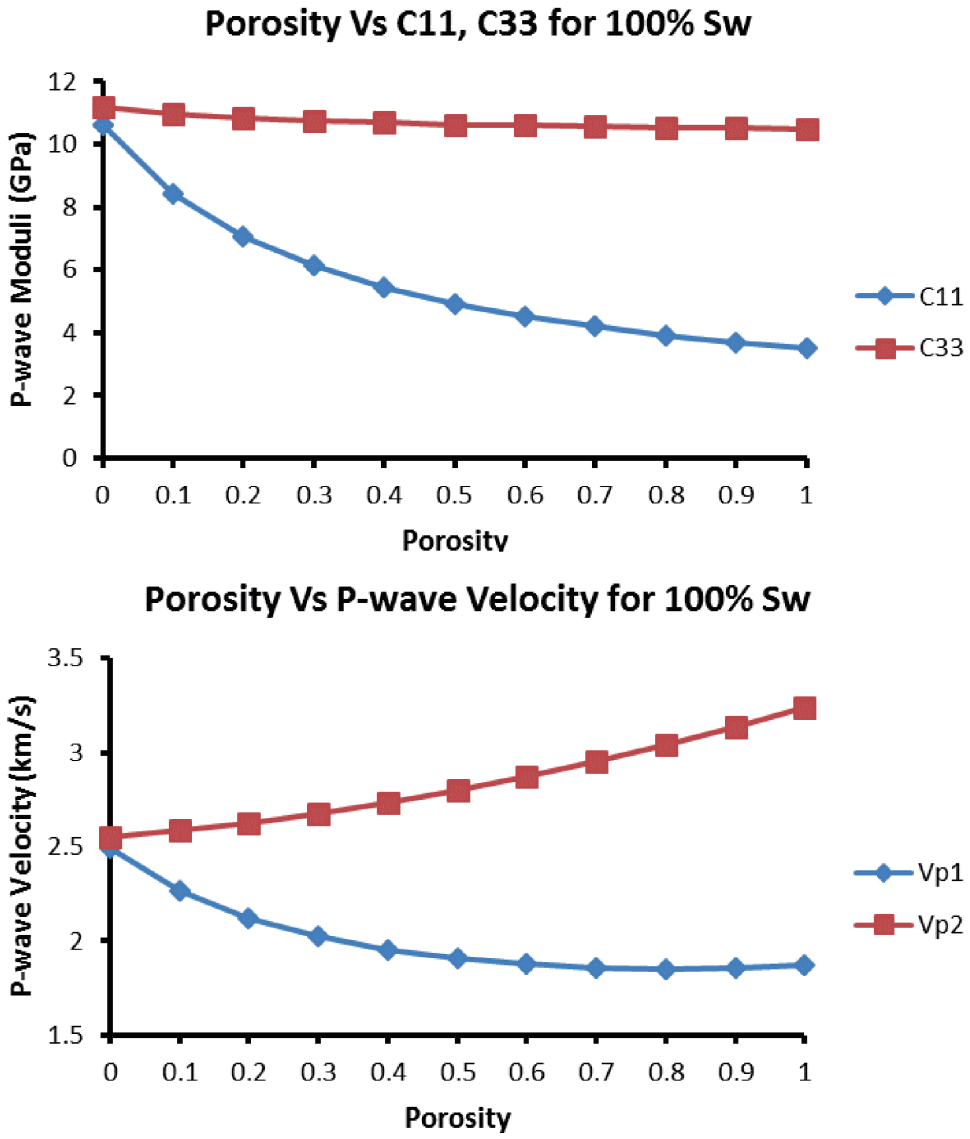

Figure 3.11: Changes in P-wave moduli ($\boldsymbol{C_{11}}$ and $\boldsymbol{C_{33}}$) with porosity (top panel). $\boldsymbol{C_{11}}$ is more sensitive to porosity change. Bottom panel shows the velocity change with increasing porosity. Note Vp2 has a different trend compared to its corresponding stiffness ($\boldsymbol{C_{33}}$). In this figure, water saturation is 100%.

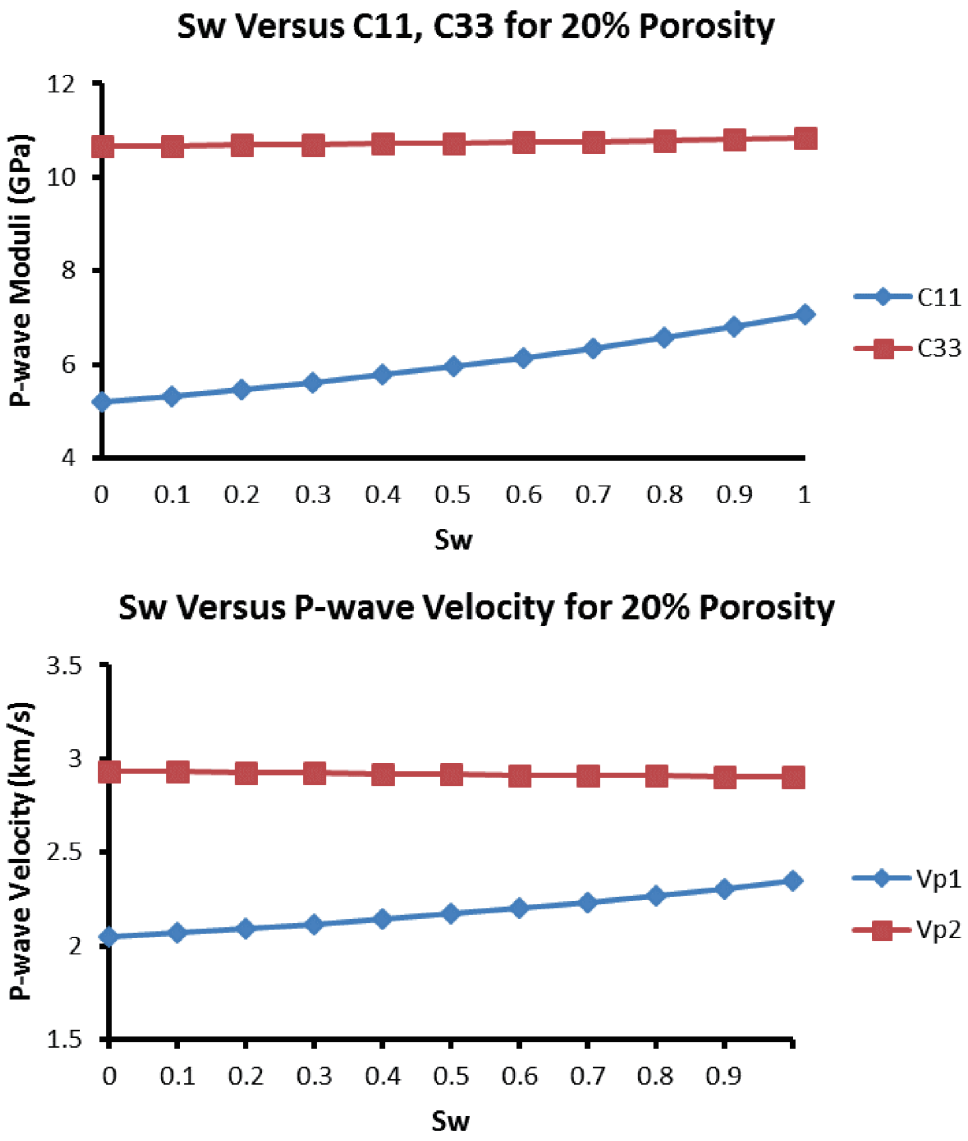

Figure 3.12: Changes in P-wave moduli ($\boldsymbol{C_{11}}$ and $\boldsymbol{C_{33}}$) as a function of water saturation (Sw) with water and oil mixture (top panel). The bottom panel shows the velocity change with increasing water saturation. The plot is made for 20% porosity case.

In Figure 3.12 (top panel), we also plot the $\boldsymbol{C_{11}}$ and $\boldsymbol{C_{33}}$ values as a function of water saturation with 20% porosity. The fluid here is a mixture of water and oil and the effective fluid bulk modulus is calculated by Reuss average with the oil bulk modulus being 1.3 GPa. As expected, P-wave moduli are increasing with water saturation and again $\boldsymbol{C_{11}}$ is more sensitive than $\boldsymbol{C_{33}}$. However, if we look at velocity changes (Figure 3.11, bottom panel), we find that Vp2 which is the P-wave traveling parallel to the fracture planes is decreasing with the increasing porosity. This is because when as the porosity increases, density decreases faster than the increase of stiffness. So the velocity increases as a result. However, for the direction normal to fracture planes, the situation is different as the change of $\boldsymbol{C_{11}}$ is much greater than density. The different trends for P-wave moduli and velocities with increasing water saturation can be explained in a similar way (Figure 3.12). We also observe from the plots that water saturation has a smaller influence on $\boldsymbol{V_{P2}}$ (or $\boldsymbol{C_{33}}$) as compared to porosity.

3.4 Experiment data analysis and discussion

The synthetic data test gives a good examination of the equations and now we try to use these new equations to explain the data we get from the previous experiment. First, we calculate the stiffness matrix of the dry (Equation 3.58) and water-saturated (Equation 3.59) printed HTI model from measurement.

$$\boldsymbol{C_{HTI}} = \begin{pmatrix} \mathbf{2.89} & \mathbf{1.53} & \mathbf{1.53} & \mathbf{0} & \mathbf{0} & \mathbf{0} \\ \mathbf{1.53} & \mathbf{3.14} & \mathbf{1.63} & \mathbf{0} & \mathbf{0} & \mathbf{0} \\ \mathbf{1.53} & \mathbf{1.63} & \mathbf{3.14} & \mathbf{0} & \mathbf{0} & \mathbf{0} \\ \mathbf{0} & \mathbf{0} & \mathbf{0} & \mathbf{0.75} & \mathbf{0} & \mathbf{0} \\ \mathbf{0} & \mathbf{0} & \mathbf{0} & \mathbf{0} & \mathbf{0.65} & \mathbf{0} \\ \mathbf{0} & \mathbf{0} & \mathbf{0} & \mathbf{0} & \mathbf{0} & \mathbf{0.65} \end{pmatrix} \boldsymbol{GPa} \tag{3.58}$$

$$\boldsymbol{C_{HTI}} = \begin{pmatrix} \mathbf{3.26} & \mathbf{1.92} & \mathbf{1.92} & \mathbf{0} & \mathbf{0} & \mathbf{0} \\ \mathbf{1.92} & \mathbf{3.42} & \mathbf{1.90} & \mathbf{0} & \mathbf{0} & \mathbf{0} \\ \mathbf{1.92} & \mathbf{1.90} & \mathbf{3.42} & \mathbf{0} & \mathbf{0} & \mathbf{0} \\ \mathbf{0} & \mathbf{0} & \mathbf{0} & \mathbf{0.76} & \mathbf{0} & \mathbf{0} \\ \mathbf{0} & \mathbf{0} & \mathbf{0} & \mathbf{0} & \mathbf{0.65} & \mathbf{0} \\ \mathbf{0} & \mathbf{0} & \mathbf{0} & \mathbf{0} & \mathbf{0} & \mathbf{0.65} \end{pmatrix} \boldsymbol{GPa} \tag{3.59}$$

Then we use our equations (Equation 3.60) and exact Gassmann's equations (Equation 3.61) to predict the stiffness change after water saturation.

$$\boldsymbol{C_{HTI}} = \begin{pmatrix} \mathbf{3.30} & \mathbf{1.84} & \mathbf{1.84} & \mathbf{0} & \mathbf{0} & \mathbf{0} \\ \mathbf{1.84} & \mathbf{3.32} & \mathbf{1.82} & \mathbf{0} & \mathbf{0} & \mathbf{0} \\ \mathbf{1.84} & \mathbf{1.82} & \mathbf{3.32} & \mathbf{0} & \mathbf{0} & \mathbf{0} \\ \mathbf{0} & \mathbf{0} & \mathbf{0} & \mathbf{0.75} & \mathbf{0} & \mathbf{0} \\ \mathbf{0} & \mathbf{0} & \mathbf{0} & \mathbf{0} & \mathbf{0.65} & \mathbf{0} \\ \mathbf{0} & \mathbf{0} & \mathbf{0} & \mathbf{0} & \mathbf{0} & \mathbf{0.65} \end{pmatrix} \boldsymbol{GPa} \tag{3.60}$$

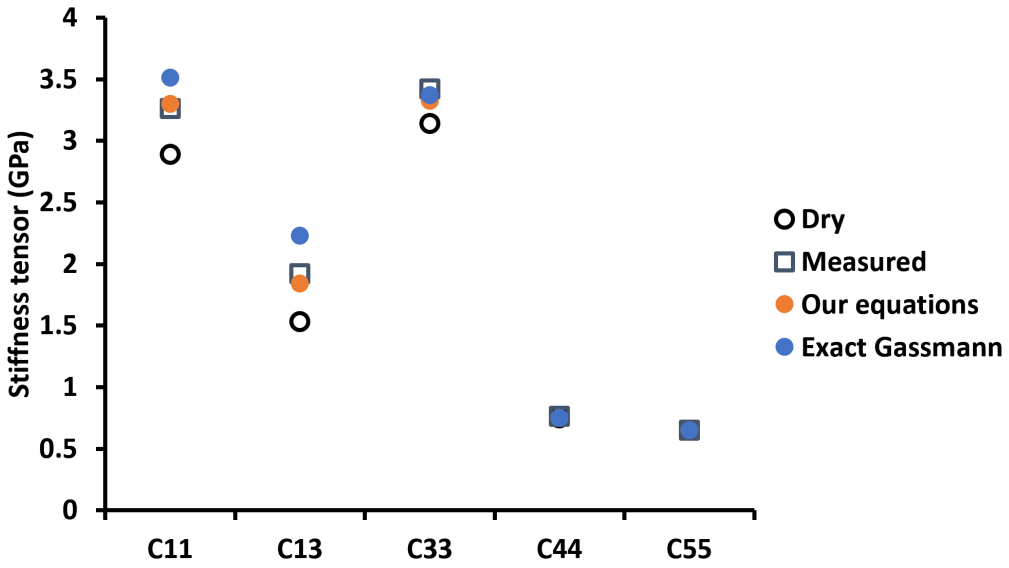

Figure 3.13: Stiffness tensors from measurements and predictions. The solid-filled markers are predictions from our new equations and exact Gassmann's equations while the unfilled markers are measured experiment data.

$$C_{HTI} = \begin{pmatrix} 3.51 & 2.23 & 2.23 & 0 & 0 & 0 \\ 2.23 & 3.37 & 1.87 & 0 & 0 & 0 \\ 2.23 & 1.87 & 3.37 & 0 & 0 & 0 \\ 0 & 0 & 0 & 0.75 & 0 & 0 \\ 0 & 0 & 0 & 0 & 0.65 & 0 \\ 0 & 0 & 0 & 0 & 0 & 0.65 \end{pmatrix} GPa \tag{3.61}$$

Figure 3.13 plots the stiffness tensors from two measurements and two predictions. The solid markers are noted as the predictions while the other two without fill are measurements. We can see that our equations can predict the stiffness change after water saturation well while the exact Gassmann's equations might not work better in this case. The velocity are also calculated (Table 3.5) and plotted (Figure 3.14)

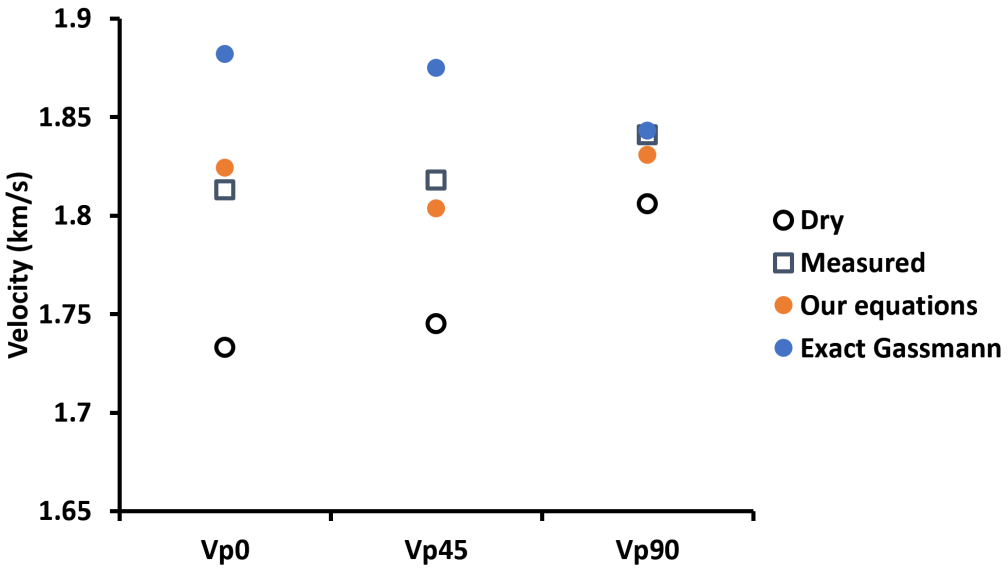

Figure 3.14: Velocities from measurements and predictions. The solid-filled markers are predictions from our new equations and exact Gassmann's equations while the unfilled markers are measured experiment data.

from the stiffness matrix.

Velocity (m/s)	V_{P0}	V_{P45}	V_{P90}	$V_{S\parallel}$	$V_{S\perp}$
Dry	1733	1745	1806	884	823
Measured	1813	1818	1841	875	810
Our equations	1824	1804	1831	870	810
Exact Gassmann	1882	1874	1843	870	810

Table 3.5: Velocity variation with measurements and predictions.

By comparing the velocity measurements and predictions, we find that both predictions from our equations and the exact Gassmann's equations match the measured velocities. But our equations match better. This is not as expected because

in theory the exact Gassmann should give the best prediction. Also we find that the exact Gassmann's equations fail on the medium symmetry after saturation. We know that the anisotropic symmetry should remain constant after fluid substitution can this is confirmed by the measured data. However, the exact Gassmann's equations predict that after water saturation, $\boldsymbol{C_{11}}$ becomes bigger than $\boldsymbol{C_{33}}$ which is not correct. Here is an possible explanation for this problem. The measured velocity, especially the 45° P-wave velocity, might not be accurate enough. Yan et al. (2012) show that the angle and velocity measurement around 45° is critical for reliable anisotropy measurement and 1% of $\boldsymbol{V_{P45}}$ can cause 40% error in $\boldsymbol{C_{13}}$. The error in $\boldsymbol{V_{P45}}$ can explain the failure of exact Gassmann which depends on the accurate measurements of stiffness tensors. Our equations and methods, however, are free of $\boldsymbol{V_{P45}}$ and thus in a sense more reliable and accurate. Also we calculate the Thomsen's parameters before and after fluid substitution to see how they change. Equation 2.4 to 2.6 are used for calculation and since the exact Gassmann's equations fail, we will not put it in further discussion. Table 3.6 shows the calculated Thomsen's parameters before and after saturation. From direct measurements, we see that $\boldsymbol{\epsilon^V}$ and $\boldsymbol{\delta^V}$ decrease 41% and 39% in magnitude respectively while $\boldsymbol{\gamma^V}$ increase 8.5% in magnitude after water saturation. Our equations predict $\boldsymbol{\delta^V}$ decreases 92% and $\boldsymbol{\epsilon^V}$ decreases 43% after saturation while $\boldsymbol{\gamma^V}$ remains constant as defined by the equations. In summary, the 3D printed models are interesting and helpful in understanding the fluid-dependence of anisotropic rocks. These models allow us to examine all kinds of different theory and methods about rock physics models. In this thesis, a new set of equations for fluid substitution for an HTI medium are derived

Thomsen's parameters	ϵ^V	δ^V	γ^V
Dry	-0.039	-0.093	-0.067
Measured	-0.023	-0.056	-0.072
Our equations	-0.003	-0.052	-0.067

Table 3.6: Thomsen's parameters of the HTI model before and after saturation.

and tested with both synthetic data and experiment data with a printed HTI model. The new equations work well for predicting elastic properties change with fluid.

Chapter 4

Conclusion

The purpose of the thesis is to characterize fracture zones through seismic data and rock physics modeling. To do this, two physical models are studied and analyzed. A laser-etched glass model is studied first. Ultrasonic velocity measurements help us understand its symmetry and it turns out to be an HTI medium. Very small velocity difference (less than 2%) between pure glass and fracture zone are observed thus reflections from the fracture zone interfaces are expected to be subtle. Two 2D lines which are on and off fracture zone, are surveyed for comparison and the raw data shows the reflections from fracture zone. Some processings for signal enhancement are done to remove linear events and to preserve and recover the true amplitude of the reflections. By comparing the processed data from on and off fracture zone, fracture zone reflections are confirmed. Then multi-component data are acquired with full azimuth coverage. From all different component data, the vertical-vertical data and horizontal-horizontal (polarised normal to survey line) data give the best signals

from the fracture zone. In order to recover the true amplitude of the reflections, radiation pattern of the transducers are studied. A theoretical equation is applied to fit the measurement and used for amplitude correction. With recovered amplitude, AVO/AVAZ analysis is performed on the vertical-vertical component data. Through reflection coefficient curve fitting and inversion, the azimuth is recovered. However, because of limited offset, more sophisticated inversion for fracture paraments are hard to perform. As for the horizontal to horizontal component data, the reflection from the fracture zone are highly contaminated by the side reflections and its true amplitude is not recovered with processing. However, since the azimuthal change in amplitude of the fracture zone reflected signals are so obvious, fracture orientation can be recovered easily with simple analysis. The converted wave signals from the fracture zone are hard to recover from data because of some problems with the model and transducers as discussed in Chapter 2. From the experiments with the glass model, reflections from fracture zone are recognized with surface seismic data. Although the reflections are very weak and contaminated with noise, careful processing helps enhance the signals a lot. Through AVO/AVAZ analysis, the fracture orientation is recovered. The other model studied in this thesis is a 3D printed HTI model. This model is directly printed with a 3D printer and ultrasonic velocity measurements show that it has an HTI symmetry but slightly orthorhombic. For simplification, the model is studied as an HTI medium. The model is found to be quite porous and permeable, a fluid substitution experiment is done. Elastic properties are measured after water saturation and significant changes are observed. There is as much as 5% increase in P-wave velocity and 2% decrease in S-wave

velocity. Changes in Thomsen's parameters are even more significant. $\boldsymbol{\epsilon^V}$ and $\boldsymbol{\delta^V}$ decrease for about 41% and 39% in magnitude respectively while $\boldsymbol{\gamma^V}$ increase 8.5% in magnitude after water saturation. To explain the changes, a new set of equations are derived based on Gassmann's equations and linear slip theory. The new equations are first tested with synthetic data and they work well. Then experiment data are analysed and explained with the new equations and the exact Gassmann's equations. The results show that Gassmann's equations fail to work well because they are quite sensitive to $\boldsymbol{V_{P45}}$ while our new equations which are free of $\boldsymbol{V_{P45}}$ work well. However, our equations could not give a very accurate prediction for the change of Thomsen's parameters. The two physical models with two novel techniques give a lot of possibilities for modeling fractured reservoirs and exhibit rich anisotropic response. The experiments with these models help us develop and test new methods and algorithms for fracture characterization and more progress is expected from these models.

References

Bakulin, A., V. Grechka, and I. Tsvankin, 2000a, Estimation of fracture parameters from reflection seismic data-part I: HTI model due to a single fracture set: Geophysics, **65**, 1788–1802.

———, 2000b, Estimation of fracture parameters from reflection seismic data-part II: Fracture models with orthorhombic symmetry: Geophysics, **65**, 1803–1817.

Bayuk, I., and E. M. Chesnokov, 1998, Correlation between elastic and transport properties of porous cracked anisotropic media: Physics and Chemistry of the Earth, **23**, 361–366.

Buddensiek, M. L., C. M. Krawczyk, N. Kukowski, and O. Oncken, 2009, Performance of piezoelectric transducers in terms of amplitude and waveform: Geophysics, **74**, T33–T45.

Calì, J., D. A. Calian, C. Amati, R. Kleinberger, A. Steed, J. Kautz, and T. Weyrich, 2012, 3d-printing of non-assembly, articulated models: ACM Trans. Graph., **31**, 130:1–130:8.

Cheadle, S. P., R. J. Brown, and D. C. Lawton, 1991, Orthorhombic anisotropy: A physical seismic modeling study: Geophysics, **56**, 1603–1613.

Ebrom, D. A., R. H. Tatham, K. K. Sekharan, J. A. McDonald, and G. H. F. Gardner, 1990, Hyperbolic traveltime analysis of first arrivals in an azimuthally anisotropic medium: A physical modeling study: Geophysics, **55**, 185–191.

Gassmann, F., 1951, Uber die elastizitat poroser medien: Veirteljahrsschrift der Naturforschenden Gesellschaft, **96**, 1–23.

Gurevich, B., 2003, Elastic properties of saturated porous rocks with aligned fractures: Journal of Applied Geophysics, **54**, WA157–WA166.

Hsu, C.-J., and M. Schoenberg, 1993, Elastic waves through a simulated fractured medium: Geophysics, **58**, 964–977.

Hudson, J. A., 1981, Wave speeds and attenuation of elastic waves in material containing cracks: Geophysical Journal of the Royal Astronomical Society, **64**, no. 1, 133–150.

Jiang, T., and E. M. Chesnokov, 2012, Elastic moduli's relation to microstructure properties in porous media using GSA modeling: SEG Technical Program Expanded Abstracts, 1–5.

Kuster, G., and M. Toksz, 1974, Velocity and attenuation of seismic waves in two-phase media: Part I. theoretical formulations: Geophysics, **39**, no. 5, 587–606.

Lemu, H. G., and S. Kurtovic, 2012, 3d printing for rapid manufacturing: Study of dimensional and geometrical accuracy: IFIP Advances in Information and Communication Technology, **384**, 470–479.

Mavko, G., and K. Bandyopadhyay, 2009, Approximate fluid substitution for vertical velocities in weakly anisotropic vti rocks: Geophysics, **74**, D1–D6.

Prioul, R., A. Donald, R. Koespsell, Z. E. Marzouki, and T. Bratton, 2007, Forward

modeling of fracture-induced sonic anisotropy using a combination of borehole image and sonic logs: Geophysics, **72**, E135–E147.

Rathore, J. S., E. Fjaer, R. M. Holt, and L. Renlie, 1995, P- and s-wave anisotropy of a synthetic sandstone with controlled crack geometry: Geophysical Prospecting, **43**, 711–728.

Rüger, A., 2001, Reflcetion coefficients and azimuthal avo analysis in anisotropic media: Society of Exploration Geophysicists.

Sayers, C. M., and M. Kachanov, 1995, Microcrack-induced elastic wave anisotropy of brittle rocks: Journal of Geophysical Research, **100**, 4149–4156.

Schoenberger, M., and C. M. Sayers, 1995, Seismic anisotropy of fractured rock: Geophysics, **60**, 204–211.

Segerman, H., 2012, 3d printing for mathematical visualisation: The Mathematical Intelligencer, **34**, no. 4, 56–62.

Shermergor, T. D., 1977, Theory of elasticity of inhomogeneous media, moscow: Nanka, (in Russian).

Sil, S., 2013, Fracture parameter estimation from well-log data: Geophysics, **78**, D129–D134.

Sil, S., M. K. Sen, and B. Gurevich, 2011, Analysis of fluid substitution in a porous and fractured medium: Geophysics, **76**, 430–458.

Smith, T. M., C. H. Sondergeld, and C. S. Rai, 2003, Gassmann fluid substitutions: A tutorial: Geophysics, **68**, 430–440.

Stewart, R. R., N. Dyaur, B. Omoboya, J. J. S. de Figueiredo, M. Willis, and S. Sil, 2013, Physical modeling of anisotropic domains: Ultrasonic imaging of laser-etched

fractures in glass: Geophysics, **78**, D11–D19.

Tatham, R. H., M. D. Matthews, K. K. Sekharan, C. J.Wade, and L. M. Liro, 1992, A physical model study of shear-wave splitting and fracture intensity: Geophysics, **57**, 647–652.

Thomsen, L., 1986, Weak elastic anisotropy: Geophysics, **51**, 1954–1966.

Yan, F., D. Han, and Q. Yao, 2012, Oil shale anisotropy measurement and sensitivity analysis: SEG Technical Program Expanded Abstracts, 1–5.